Second-harmonic generation in Mie-resonant dielectric nanoparticles made of noncentrosymmetric materials

Kristina Frizyuk,[1] Irina Volkovskaya,[2] Daria Smirnova,[2] Alexander Poddubny,[1,3] and Mihail Petrov[1]
[1]*ITMO University, St. Petersburg 197101, Russia*
[2]*Institute of Applied Physics, Russian Academy of Sciences, Nizhny Novgorod 603950, Russia*
[3]*Ioffe Institute, St. Petersburg 194021, Russia*

(Received 5 October 2018; revised manuscript received 30 January 2019; published 19 February 2019)

We develop a multipolar theory of second-harmonic generation (SHG) by dielectric nanoparticles made of noncentrosymmetric materials with bulk quadratic nonlinearity. We specifically analyze two regimes of optical excitation: illumination by a plane wave and single-mode excitation, when the laser pump drives the magnetic dipole mode only. Considering two classes of nonlinear crystalline solids (dielectric perovskite material and III-V semiconductor), we apply a symmetry approach to derive selection rules for the multipolar composition of the nonlinear radiation. The developed description can be used for design of efficient nonlinear optical nanoantennas with reconfigurable radiation characteristics.

DOI: 10.1103/PhysRevB.99.075425

I. INTRODUCTION

The resonant response is one of the main routes to increase the efficiency of nonlinear signal generation at the subwavelength scales in the absence of phase matching effects. That is why optical nonlinearity at the nanoscale is usually associated with the enhancement of electric fields in plasmonic nanostructures due to geometric plasmon resonances [1,2]. Despite the significant progress in this area [3], there exist fundamental drawbacks that limit the efficiency of nonlinear generation with metallic structures. Besides the evident problem of high ohmic losses, typical metals have cubic lattice with inversion symmetry which restricts second-order nonlinear effects, such as the second-harmonic generation (SHG) [4]. It can be observed only due to the surface effects or the field gradients in the bulk of nanoparticles [3,5], which are relatively weak. Recently, a novel nanophotonic platform based on high-index dielectric nanoparticles has emerged [6]. All-dielectric nanostructures are free from high ohmic losses and offer a wide variety of dielectric and semiconductor materials including those with nonzero bulk second order susceptibility tensor. Excitation of Mie resonances in such nanoparticles provides novel opportunities for nonlinear optics [7,8] and allows one to achieve record-high nonlinear conversion efficiencies at the nanoscale [9–15].

Despite the intense experimental studies of the SHG effects in Mie-resonant nanostructures, a comprehensive theory of the SHG emission from nanoparticles with nonzero bulk nonlinearity tensor $\hat{\chi}^{(2)}$ has not been proposed yet. The important works related to the SHG generation were focused on the surface and bulk effects in nanoparticles with centrosymmetric crystalline lattice: in noble metal nanoparticles [16–18] including the shape effects [19], and in Mie-resonant silicon nanoparticles [20,21]. In this work, we theoretically study the SHG by individual spherical high-index dielectric nanoparticles made of noncentrosymmetric materials (aluminum gallium arsenide AlGaAs and barium titanate $BaTiO_3$), which possess a large bulk quadratic susceptibility. These materials are actively employed for nonlinear all-dielectric nanophotonics [9,11,22–24]. We systematically describe the SHG in nanoparticles and mechanisms of its resonant enhancement, depending on the symmetry of the crystalline structure and polarization of the incident light. We employ methods of multipolar electrodynamics providing a transparent interpretation for the measurable far-field characteristics, such as radiation efficiency and radiation patterns [7,21,25].

Using analytical techniques, we demonstrate the ability to manipulate the nonlinear radiation of a spherical nanoparticle by varying illumination properties. By means of symmetry analysis of the SHG process we obtain the selection rules for the nonlinear generation, and identify which channels of multipole composition are active in SHG. These rules previously were known only for nanoparticles of a spherical [16] and arbitrary shape [19] made of centrosymmetric materials. The knowledge of these basic mechanisms of nonlinear generation in a single spherical nanoparticle can be extended in application to complex nonlinear structures, such as nanoparticle oligomers [26,27] or nanoparticle arrays in metasurfaces [8].

The paper is organized as follows: In Sec. II we discuss the problem of nonlinear light scattering of a plane wave by a dielectric nanoparticle made of $BaTiO_3$ or AlGaAs materials. Applying Green's function approach, we calculate the efficiency of SHG and multipolar content of the second-harmonic (SH) field. We also consider the particular case of SHG through excitation of a single magnetic dipole mode. We discuss how the intensity and the far-field properties of the SH field vary while direction of the excited dipole moment changes relatively to the crystalline structure of material. By explicit calculations we show how the mode content of SH field varies. In Sec. III we derive selection rules which govern the channels of mode coupling at fundamental and SH wavelengths based on the symmetry of vector spherical harmonics and the crystalline structure. In Sec. IV we apply the formulated selection rules to explain the results obtained

in Sec. II and build the complete table of possible generated multipoles for SHG process driven by dipole modes.

II. SECOND-HARMONIC GENERATION FORMALISM

A. Green's function approach. Plane-wave excitation

We consider a spherical dielectric particle of the radius a characterized by a frequency-dependent dielectric permittivity $\varepsilon_2(\omega)$, embedded in a homogeneous host medium with $\varepsilon_1 = 1$. The nanoparticle is made of the material with a noncentrosymmetric crystalline structure, and its nonlinear electromagnetic properties are captured by the quadratic susceptibility tensor $\hat{\chi}^{(2)}$. While for AlGaAs the linear susceptibility tensor $\varepsilon_2(\omega)$ is isotropic, for $BaTiO_3$ this tensor inherits the uniaxial crystal structure of the material. In this case, the anisotropy of the SHG tensor and of the linear permittivity tensor are not two independent phenomena and have a common microscopic origin [28]. However the anisotropy is rather weak in the case of $BaTiO_3$; it dramatically increases the complexity of the problem comparing to isotropic linear scattering. Hence, from now on we use the approximation of isotropic linear susceptibility tensor. The effect of anisotropy on the selection rules will be discussed in more details at the end of the paper in Sec. IV.

The problem of linear light scattering by a sphere is solved using the multipolar expansion following the Mie theory [29,30]. In our work we consider time dependence of the fields in the form $e^{-i\omega t}$. For the illumination by the x-polarized plane wave $E_0 \boldsymbol{e}_x e^{ik_1 z}$ incident along the z direction, the field inside the spherical nanoparticle ($r < a$) is expanded in vector spherical harmonics as follows:

$$\mathbf{E}^{\omega}(\mathbf{r}) = \sum_{n=1}^{\infty} i^n \frac{(2n+1)}{n(n+1)} \big[c_n \mathbf{M}^{(1)}_{o1n}(k_2(\omega), \mathbf{r}) - i d_n \mathbf{N}^{(1)}_{e1n}(k_2(\omega), \mathbf{r}) \big], \tag{1}$$

where the wave numbers $k_1(\omega) = \omega\sqrt{\varepsilon_1}/c$, $k_2(\omega) = \omega\sqrt{\varepsilon_2(\omega)}/c$. Magnetic $\mathbf{M}_{o1n}$ and electric $\mathbf{N}_{e1n}$ spherical harmonics with the total angular momentum n and the momentum projection ± 1, the indexes e, o describing their parity with respect to the reflection along y axis (or $\varphi \to -\varphi$ transformation), and the coefficients c_n, d_n are given in Appendix A; the superscript (1) is used to define spherical Bessel functions.

The induced nonlinear polarization at the second-harmonic frequency is defined by the second-order polarizability tensor:

$$P^{2\omega}_{\alpha}(\mathbf{r}) = \varepsilon_0 \chi^{(2)}_{\alpha\beta\gamma} E^{\omega}_{\beta}(\mathbf{r}) E^{\omega}_{\gamma}(\mathbf{r}), \tag{2}$$

where E^{ω}_{α} are the Cartesian components of the fundamental field inside the nanoparticle. We take into account only the bulk nonlinear response leaving outside the consideration potential surface sources of SHG. The SH field outside the particle at $r > a$ can be found using dyadic Green's function $\widehat{\mathbf{G}}$ of a sphere:

$$\mathbf{E}^{2\omega}(\mathbf{r}) = (2\omega)^2 \mu_0 \int_V dV' \widehat{\mathbf{G}}(2\omega, \mathbf{r}, \mathbf{r}') \mathbf{P}^{2\omega}(\mathbf{r}'), \tag{3}$$

satisfying the following equation $\mathrm{rot}\,\mathrm{rot}\,\hat{\mathbf{G}}(\omega, \mathbf{r}, \mathbf{r}') = (\frac{\omega}{c})^2 \varepsilon(\mathbf{r}, \omega) \hat{\mathbf{G}}(\omega, \mathbf{r}, \mathbf{r}') + \hat{\mathbf{1}} \delta(\boldsymbol{r} - \boldsymbol{r}')$, where $\hat{\mathbf{1}}$ is the unit dyadic, $\varepsilon(\mathbf{r}, \omega) = \varepsilon_2(\omega)$ for $r < a$, and $\varepsilon(\mathbf{r}) = 1$ for $r > a$.

The explicit multipole decomposition of the Green function is given in Ref. [31] and also in Appendix A. Substituting the expansion of the Green function in the form of the spherical waves into Eqs. (2) and (3) we obtain the multipolar decomposition of the second harmonic field

$$\mathbf{E}^{2\omega}(\mathbf{r}) = \sum_{n=1}^{\infty} \sum_{m=0}^{n} \sum_{W=M,N} E_0 \big(D_{Wemn} \mathbf{W}^{(3)}_{emn}[k_1(2\omega), \mathbf{r}] + D_{Womn} \mathbf{W}^{(3)}_{omn}[k_1(2\omega), \mathbf{r}] \big). \tag{4}$$

Here, the denotation $W = M, N$ distinguishes between electric and magnetic harmonics; the superscript (3) is used to define spherical Hankel functions of the first kind. The expansion coefficients $D_{W^e_o mn}$ are readily evaluated as a sum of overlap integrals between the two vector spherical harmonics at the ω frequency and one harmonic at the 2ω frequency, weighted by the $\widehat{\chi}^{(2)}$ tensor:

$$D_{W_{e_o^{mn}}} \sim \int_V \mathbf{W}^{(1)}_{e_o^{mn}}[k_2(2\omega), \mathbf{r}] \widehat{\chi}^{(2)} \mathbf{E}^{\omega}(\mathbf{r}) \mathbf{E}^{\omega}(\mathbf{r}) dV \,. \tag{5}$$

The explicit form of these coefficients is given in Appendix A.

Finally, the second-harmonic conversion efficiency σ_{SH}, defined as the ratio of the total SH radiated power $\mathcal{P}_{SH}$ to the energy flux of the fundamental wave I_0 through the geometrical cross section πa^2 of the particle, can be expressed through the coefficients $D_{W^e_o mn}$ as follows [32]:

$$\sigma_{\mathrm{SH}} = \frac{\mathcal{P}_{SH}}{\pi a^2 I_0} = \frac{2\pi}{\pi a^2 [k_1(2\omega)]^2} \sum_{n=1}^{\infty} \sum_{W=M,N} \frac{n(n+1)}{(2n+1)} \times \left[\sum_{m=1}^{n} \frac{(n+m)!}{(n-m)!} (|D_{Wemn}|^2 + |D_{Womn}|^2) + 2|D_{We0n}|^2 \right]. \tag{6}$$

Using Eq. (6), we calculate the conversion efficiency σ_{SH} for $BaTiO_3$ and AlGaAs particles of subwavelength sizes under the plane-wave excitation. In this section, we assume that the main axes of crystalline lattice are oriented along the coordinate system: $[100] \| \mathbf{e}_x$, $[010] \| \mathbf{e}_y$, $[001] \| \mathbf{e}_z$ (see Fig. 1). In Sec. IV we will discuss other crystalline orientations. In the chosen coordinate system the second-order polarization of the $BaTiO_3$ crystal has the following form:

$$\begin{pmatrix} P^{2\omega}_x \\ P^{2\omega}_y \\ P^{2\omega}_z \end{pmatrix} = \varepsilon_0 \begin{pmatrix} 0 & 0 & 0 & 0 & d_{15} & 0 \\ 0 & 0 & 0 & d_{15} & 0 & 0 \\ d_{31} & d_{31} & d_{33} & 0 & 0 & 0 \end{pmatrix} \times \begin{pmatrix} E^{\omega}_x E^{\omega}_x \\ E^{\omega}_y E^{\omega}_y \\ E^{\omega}_z E^{\omega}_z \\ 2E^{\omega}_y E^{\omega}_z \\ 2E^{\omega}_x E^{\omega}_z \\ 2E^{\omega}_x E^{\omega}_y \end{pmatrix}, \tag{7}$$

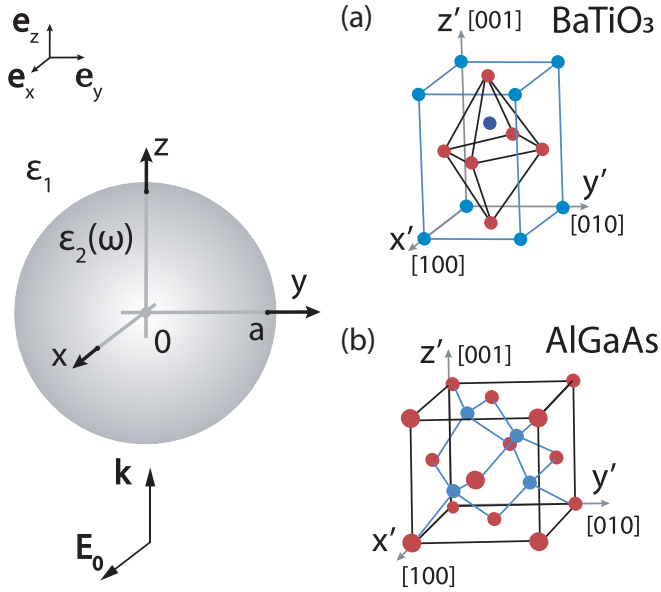

FIG. 1. Geometry of the considered problem. The crystalline lattice structure of materials under the consideration, $BaTiO_3$ (a) and AlGaAs (b), is also shown in figure. The orientation of crystalline lattice is with respect to the coordinate system fixed throughout the paper if else is not specified.

where $\chi_{zzz} = d_{33} = 6.8$ pm/V, $\chi_{zxx} = \chi_{zyy} = d_{31} = 15.7$ pm/V, $\chi_{xxz} = \chi_{yyz} = d_{15} = 17$ pm/V [33]. In the principal axis system of the AlGaAs crystal, the tensor of the second-order nonlinear susceptibility contains only off-diagonal elements $\chi^{(2)}_{ijk} \equiv \chi^{(2)} = 100$ pm/V being nonzero if any of two indices i, j, k do not coincide:

$$\begin{pmatrix} P_x^{2\omega} \\ P_y^{2\omega} \\ P_z^{2\omega} \end{pmatrix} = 2\varepsilon_0 \chi^{(2)} \begin{pmatrix} E_y^{\omega} E_z^{\omega} \\ E_x^{\omega} E_z^{\omega} \\ E_x^{\omega} E_y^{\omega} \end{pmatrix}. \tag{8}$$

The fundamental wavelengths are fixed for $BaTiO_3$ and AlGaAs to 1050 nm and 1550 nm, respectively. These values were chosen in accordance with the typical experimental frequencies used for observation of SHG from these materials and correspond to the Yb^{+3} laser (1050 nm) [23] or the Er^{+3} doped fiber laser (1550 nm) [9]. Since AlGaAs has a higher refractive index (∼3.5) compared to $BaTiO_3$ (∼2.4), the particle sizes are within the same range.

The calculated dependences of SHG on the nanoparticle radius are shown in Figs. 2(a) and 3(a) demonstrating pronounced resonant structure. In order to distinguish between different multipolar resonances, we have separately calculated the contribution from each multipolar channel in Eq. (6) [see the colored curves in Fig. 2(a) and Fig. 3(a)]. The contributions of the harmonics with the same total angular momentum n and different momentum projections m are combined together. Identification of the harmonics with particular momentum projection contributing to the SH emission will be discussed in detail in Sec. IV (see Tables III, IV, V). We also support the SH spectra with the plot of the linear scattering spectra of a plane wave at the fundamental and SH wavelengths in Figs. 2 and 3(b), clearly showing individual Mie resonances.

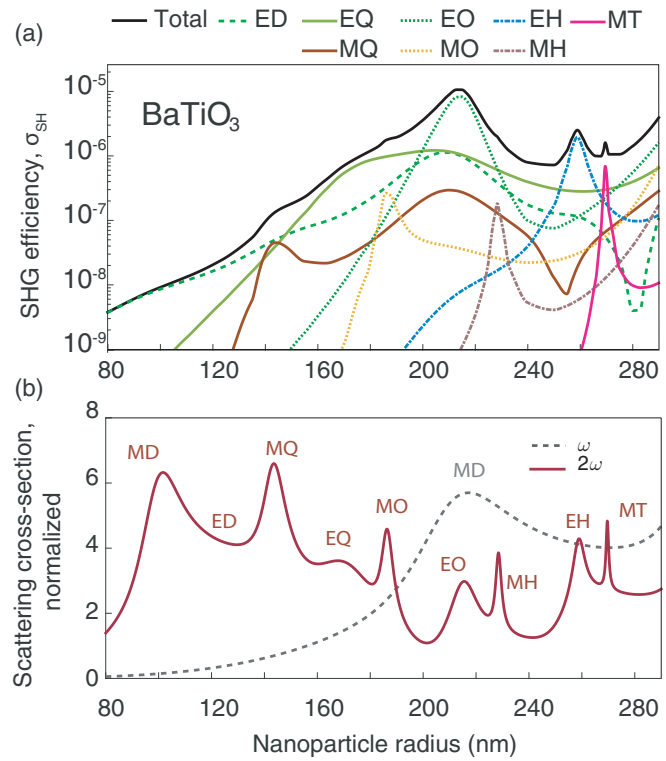

FIG. 2. Second harmonic generation spectra for $BaTiO_3$ calculated at the normal incidence, according to Fig. 1. Incident wave wavelength is 1050 nm. (a) Solid black line shows the total SH intensity, normalized to the incident power $I_0 = 10^{13}$ W/m^2 and the geometric cross section πa^2. Colored lines show different multipole contributions to the second harmonic field. (b) Scattering cross section, normalized to the geometric cross section for the two wavelengths: 1050 nm (dashed line) and 525 nm (solid line), to show the positions of the multipole resonances. E/MD—electric/magnetic dipole, Q—quadrupole, O—octupole, H—hexadecapole, T—triacontadipole.

One can see that the peaks at the SH wavelength are modulated with the broad resonance at the fundamental wavelength, which is clearly seen by comparing the panels (a) and (b) in Fig. 2 and Fig. 3. As a result, the SHG efficiency increases by several orders of magnitude when approaching the magnetic dipole (MD) resonance at the fundamental wavelength [34,35]. The dramatic enhancement is observed when the double-resonance condition is fulfilled [36–38] for instance at electrical octupole (EO) resonance [see Figs. 2 and 3(a)]. Results of our analytical calculations are confirmed by full-wave numerical modeling performed with the finite-element solver COMSOL Multiphysics, following the procedure applied in Refs. [9,21,22,25]. The multipolar amplitude coefficients are then numerically retrieved and reproduce Figs. 2 and 3.

The magnitude of the SH conversion efficiency is intensity-dependent $\sigma_{SH} \sim I_0$, as it describes the two-photon process. Specifically, for a given intensity of the incident wave of $I_0 = 1$ GW/cm^2 the conversion efficiency reaches the value of 10^{-5} for $BaTiO_3$ nanoparticle and 5×10^{-4} for AlGaAs nanoparticles in the same radius range of around 200 nm. These values are about one order of magnitude higher than the experimental values measured for nanodisks in similar experimental conditions [9,12]. This discrepancy can be related to

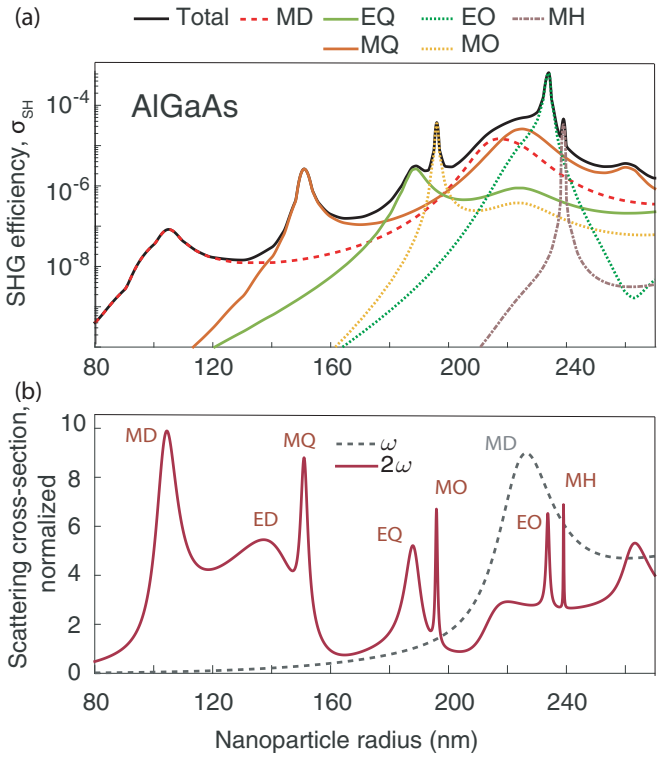

FIG. 3. Second harmonic generation spectra for AlGaAs at the normal incidence, according to Fig. 1. Incident wavelength is 1550 nm. (a) Solid black line shows the total SH intensity, normalized to the incident power $I_0 = 10^{13}$ W/m^2 and the geometric cross section πa^2. Colored lines are multipoles contributions into the SH intensity. (b) Scattering cross section, normalized to the geometric cross section for the two wavelengths: 1550 nm (dashed line) and 775 nm (solid line), to show the positions of multipole resonances. E/MD—electric/magnetic dipole, Q—quadrupole, O—octupole, H—hexadecapole, T—triacontadipole.

the lower SHG efficiency from disk resonators studied in the experiments due to the substrate effects and the uncertainty of retrieving of the efficiency value from experimental data.

Another important feature is the particular multipolar content of the SH field. For instance one can notice that the MD is absent in the SH field generated in the $BaTiO_3$ nanoparticle, and no electric dipole (ED) field is generated in the AlGaAs nanoparticle. This cancellation is dictated by the symmetry of the $\hat{\chi}^{(2)}$ tensor and direction and polarization of the fundamental wave. It will be further illustrated in Sec. II B, studied in detail from the symmetry point of view in Sec. III, and discussed in Sec. IV.

B. Single-mode approximation

Here, we specifically focus on the SHG driven by the MD mode only. In the vicinity of pronounced resonances, the field distribution inside the particle excited by the fundamental wave can be approximated by the corresponding eigenmode [21,25]. Selective and enhanced coupling to specific multipole modes can be facilitated by the beam engineering [39,40]. If the refractive index is high enough, $k_1(\omega)a\sqrt{\varepsilon_2(\omega)} \sim \pi$, the fundamental MD resonance dominates in the fundamental

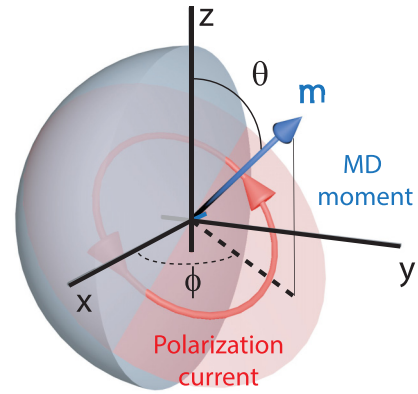

FIG. 4. The geometry of the magnetic dipole mode excitation in the nanoparticle and corresponding angles of dipole moment rotation.

field in a particular spectral region (around 220 nm radius for the fundamental wavelengths in Fig. 2 and Fig. 3). The case of SHG driven by MD excitation represents an instructive example for understanding the multipolar nature of the generated electromagnetic fields in Mie-resonant dielectric nanoparticles.

We employ a single-mode approximation and assume that the field inside the AlGaAs nanoparticle at $r < a$ is given by a MD mode profile with the y-aligned magnetic moment:

$$\mathbf{E}_M^{\omega}(\mathbf{r}) = E_0 \frac{3ic_1}{2} \mathbf{M}_{o11}^{(1)}(k_2(\omega), \mathbf{r}). \tag{9}$$

This geometry corresponds to $\mathbf{m}||\mathbf{e}_y$ or $\theta = \pi/2, \varphi = \pi/2$ in Fig. 4. Integration of the trigonometric functions in Eq. (5) over the angles shows that within the framework of single-mode MD approximation (9) and crystalline axes of material oriented according to Fig. 1, the multipolar composition features electric octupole and magnetic quadrupole for the AlGaAs nanoparticle, allowing us to write down the expression for the field:

$$\mathbf{E}^{2\omega}(r > a) = E_0\big[D_{N_{o23}}\mathbf{N}_{o23}^{(3)}(k_1(2\omega), \mathbf{r}) + D_{M_{e02}}\mathbf{M}_{e02}^{(3)} \times (k_1(2\omega), \mathbf{r}) + D_{M_{e22}}\mathbf{M}_{e22}^{(3)}(k_1(2\omega), \mathbf{r})\big]. \tag{10}$$

The multipolar amplitudes D_{No23}, D_{Me02}, and D_{Me22} can be also conveniently found using the *Lorentz lemma* following the procedure described in Ref. [21], being alternative to the Green's function integration in Sec. II A. This allows us to write the expression for D amplitudes through transmission coefficient $t_n^{E,M}(a)$ (see Ref. [21]) of the incident spherical wave irradiating the particle. After some algebra, we obtain compact analytical expressions for the multipolar coefficients:

$$\begin{aligned} D_{Me02} &= \frac{-36i\sqrt{30\pi}\,\chi^{(2)} t_2^M(k_2a)}{5\varepsilon_2(\omega)^{3/2}} I_2 E_0 c_1 (k_2a)^2 O_{02}, \\ D_{Me22} &= \frac{18i\sqrt{20\pi}\,\chi^{(2)} t_2^M(k_2a)}{5\varepsilon_2(\omega)^{3/2}} I_2 E_0 c_1 (k_2a)^2 O_{22}, \\ D_{No23} &= \frac{72\sqrt{70\pi}\,\chi^{(2)} t_3^E(k_2a)}{35\varepsilon_2(\omega)\varepsilon_2(2\omega)} \sqrt{\frac{\varepsilon_2(2\omega)}{\varepsilon_2(\omega)}} I_2 E_0 c_1 (k_2a)^2 O_{23}, \end{aligned} \tag{11}$$

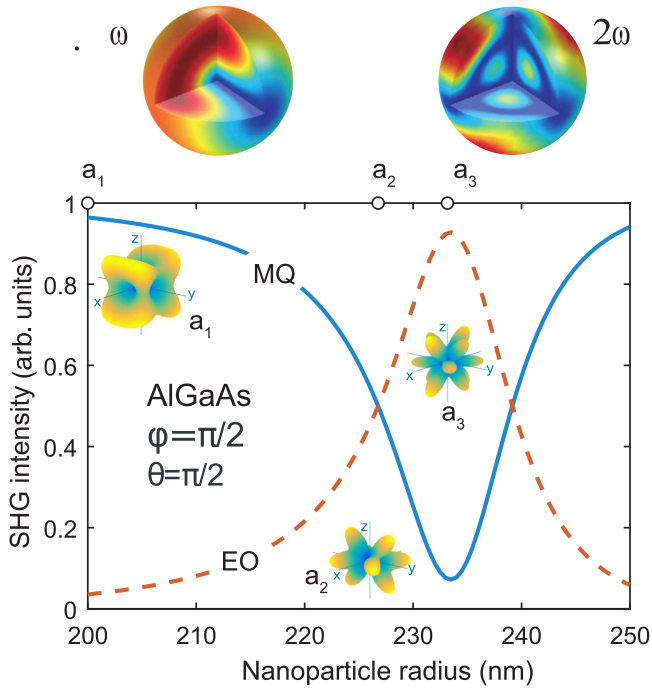

FIG. 5. SHG conversion efficiency decomposed into relative magnetic quadrupolar (blue solid line) and electric octupolar (red dashed line) contributions in the AlGaAs nanoparticles at the pump wavelength of 1550 nm. Insets show the far-field SH radiation patterns at $a_1 = 200$ nm, $a_2 = 227$ nm, $a_3 = 234$ nm. The top figure shows the field distribution inside the nanoparticle of radius $a_2 = 227$ nm at the fundamental and SH frequencies.

where

$$I_2(k_2a) = \int_0^{k_2a} j_1^2(x) j_2\left(2\sqrt{\frac{\varepsilon_2(2\omega)}{\varepsilon_2(\omega)}}x\right)x^2dx,$$

$$O_{mn} = \frac{1}{\sqrt{n(n+1)}}\sqrt{\frac{(2n+1)}{4\pi}\frac{(n-m)!}{(n+m)!}}.$$

The relative contribution of different multipoles varies when the SH wavelength is tuned to corresponding Mie resonances. This immediately follows from the expressions for multipolar amplitudes Eq. (11). In Fig. 5 we trace this behavior by plotting the dependence of the SH intensity on nanoparticle size. When the radius is increased, the contribution of EO mode starts to dominate over the magnetic quadrupole (MQ) changing the far-field radiation pattern from axially symmetric for smaller particles to the multilobed pattern near the EO resonance at $a = 234$ nm. The field distribution inside the nanoparticle (see insets in Figs. 5–7) was obtained with the help of COMSOL Multiphysics package. The radiation patterns (see insets in Figs. 5–8), showing the distribution of the generated SH intensity in the far field, were plotted with the use of the formula Eq. (4) and were verified numerically by full-wave calculations in COMSOL.

Rotation of the pump magnetic dipole in the xy plane ($\theta = \pi/2$ in Fig. 4) enables the generation of the ED mode in AlGaAs nanoparticle, which is also illustrated in Table I. The presence of the specific modes in the SH spectrum will

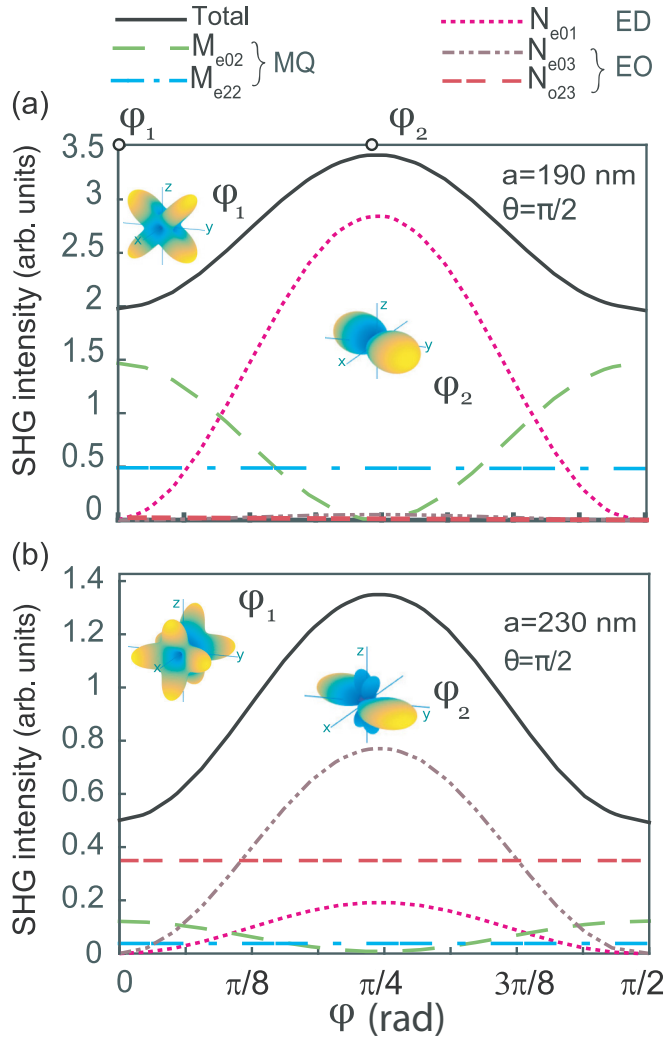

FIG. 6. Dependence of the SH intensity and generated multipoles on the pump magnetic dipole rotation by angle φ in the xy plane ($\theta = \pi/2$) in AlGaAs particles of two radii $a = 190$ nm (a), 230 nm (b) at the pump wavelength 1550 nm. Insets show the SH radiation patterns at $\varphi_1 = 0$, $\varphi_2 = \pi/4$.

be discussed in detail in Sec. IV based on symmetry reasons. For the smaller nanoparticle of $a = 190$ nm [Fig. 6(a)], being remote from the EO-resonant size, the EO contribution in the SH field is negligible. At $\varphi = 0$ or $\pi/2$, the SH radiation is dominated by the magnetic quadrupole. If the pump magnetic dipole is rotated by $\varphi = \pi/4$, the ED relative contribution exceeds MQ and the radiation pattern significantly changes. For the larger nanoparticle of $a = 230$ nm [Fig. 6(b)], the EO term dominates in the SH emission.

The results of analogous calculations for $BaTiO_3$ particle are summarized in Fig. 7. Here, two different orientations of the magnetic dipole ($\varphi = \pi/2$, $\theta = 0$ and $\varphi = \pi/2$, $\theta = \pi/2$) are shown and the resonant switching between dipolar, quadrupolar, and octupolar modes is observed.

In Fig. 8 we illustrate the effect of the MD rotation in the yz plane ($\varphi = \pi/2$) for the $BaTiO_3$ particle of radius $a = 140$ nm, corresponding to the MQ peak in Fig. 3(b). Rotation of MD in the xy plane will not give any changes due to symmetry

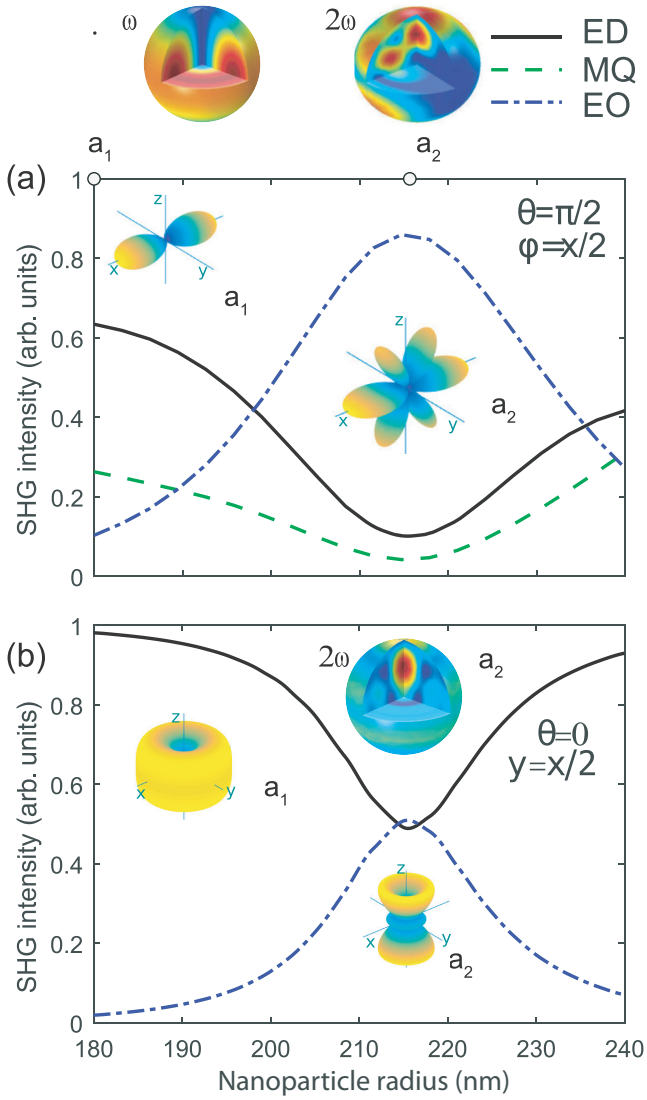

FIG. 7. Dependence of the SH intensity in $BaTiO_3$ particles on the nanoparticle radius decomposed into relative electric dipolar (ED), magnetic quadrupolar (MQ), electric octupolar (EO) contributions at the pump magnetic dipole wavelength of 1050 nm for $\varphi = \pi/2$, $\theta = \pi/2$ (a), and $\theta = 0$ (b). The insets show far field patterns of SH radiation for nanoparticle sizes $a_1 = 180$ nm and $a_2 = 214$ nm. The field distributions inside a nanoparticle are shown for the fundamental and SH wavelengths for nanoparticle radius a_2.

of $BaTiO_3$ lattice with respect to this rotation. At $\theta = 0$ the induced nonlinear source does not contain a MQ component, and, thus, weak SHG is determined by the nonresonant ED. When the angle θ is increased, the total SHG intensity grows and the leading contribution to the SH radiation originates from the resonant MQ.

III. SYMMETRY ANALYSIS FOR THE SECOND-HARMONIC GENERATION

In this section, we analyze the possibility of SHG through different multipole channels which is determined by the particular symmetry of modes at the fundamental and SH

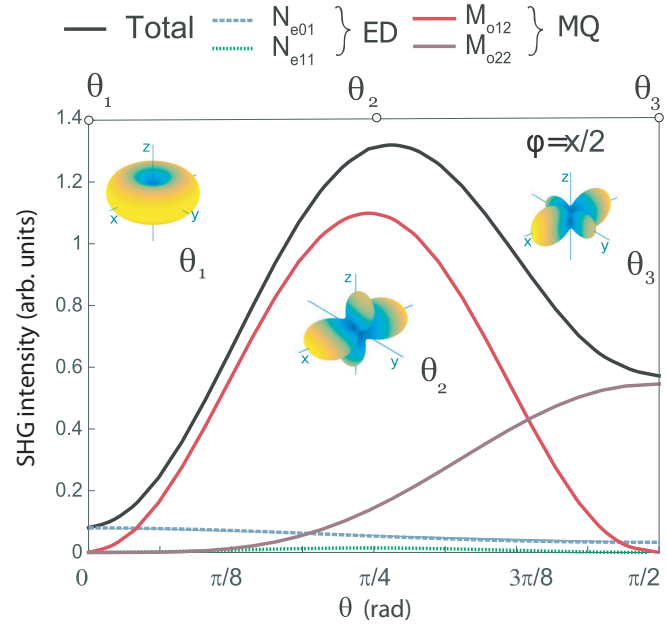

FIG. 8. Dependence of the SH intensity and generated multipoles on the pump magnetic dipole rotation by angle θ in the yz plane ($\varphi = \pi/2$) in $BaTiO_3$ particle of radius $a = 140$ nm. Insets show SH radiation patterns at $\theta_1 = 0$, $\theta_2 = \pi/4$, $\theta_3 = \pi/2$.

frequencies. The integrals over the nanoparticle volume

$$I_{\mu n,\mu' n' \to \mu'' n''} = \int_{r<a} dV\, \chi^{(2)}_{\alpha\beta\gamma} W^{(1)}_{\alpha,\mu n}(\boldsymbol{r}) W^{(1)}_{\beta,\mu' n'}(\boldsymbol{r}) W^{(1)}_{\gamma,\mu'' n''}(\boldsymbol{r}) \tag{12}$$

determine the contributions of the multipoles $\mu' n'$, μn to the SHG expansion coefficients $D_{W^{e}_{o} mn}$ in Eq. (5). Here, the indices μ, μ', μ'' stand for the parity e, o and the projection m of vector spherical harmonics $\mathbf{W}^{(1)}_{e/o\,mn}(\mathbf{r})$. For each particular value of indices such integrals can be readily calculated analytically, and a large number of them turn out to be zero. Our goal is to reveal the general origin of these cancellations. All our considerations are based on the following general theorem [41,42]. Let $\psi_i^{(\alpha)}$ be one of the basis functions of an irreducible (nonunit) representation α of a system's symmetry group. Then the integral of this function over the configuration space of the physical system vanishes identically: $\int \psi_i^{(\alpha)} dq = 0$. In order for the integral to be nonzero, the integrand must contain a term that is invariant when any of the symmetry operations of the group are applied, otherwise the integral vanishes.

TABLE I. Single-mode excitation. Generated nonlinear multipoles in AlGaAs nanoparticle for two orientations of the pump MD moment under the rotation in the xy plane ($\theta = \pi/2$). The shaded region coincides with the shaded region in Table V.

pump MD	SHG
$\varphi = \pi/2$ (m_y)	MQ, EO M_{e02}, M_{e22}, N_{o23}
$\varphi = \pi/4$ $(m_x = m_y)$	ED, MQ, EO N_{e01}, M_{e22}, N_{e03}, N_{o23}

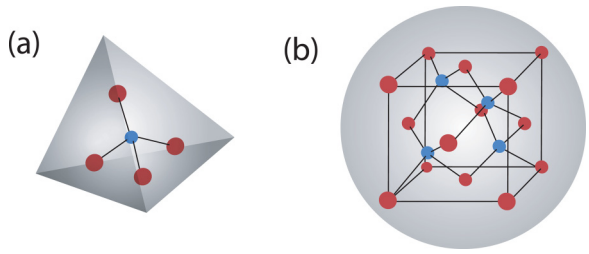

FIG. 9. Schematic illustration of (a) an atomic cluster with T_d symmetry and (b) a spherical nanoparticle made of material with T_d crystalline symmetry. Cation and anion atoms are shown by blue and red color, respectively.

In the considered case, the cancellations stem from both (i) the microscopic crystalline symmetry of the material and (ii) from the macroscopic spherical symmetry of the nanoparticle as a whole. In order to illustrate this distinction, we show in Fig. 9(a) a tetrahedral nanoparticle cut from a material with T_d point group symmetry, e.g., AlGaAs, and in Fig. 9(b) the spherical nanoparticle made of the crystal with T_d point group symmetry. Then, since a tetrahedron has the same T_d symmetry, all the allowed transitions will be defined by the crystalline symmetry only. However, spherical symmetry of the nanoparticle in Fig. 9(b) imposes additional restrictions on the second harmonic generation, absent in a tetrahedron. The restrictions are provided by a certain parity of sphere eigenmodes with respect to the symmetry transformations of a sphere. Hence, we can make use of selection rules based on spatial parity of eigenmodes. As such, most of the cancellations of the integrals Eq. (12) stem from simple spherical symmetry considerations, discussed in the following Sec. III A. The rest of the relevant cancellations can be explained as inherited from the crystal point group symmetry and will be considered in Sec. III B.

We note that in our consideration we neglect the roughness of the spherical particle surface imposed by the crystalline structure as we assume nanoparticle containing large enough number of atoms. The possible nonlocal corrections to the linear dielectric response of the nanoparticle, arising from the spatial dispersion of the permittivity, and sensitive to the difference between tetradehral and spherical symmetry [43], are also neglected here, and the particle is described by the local isotropic permittivity tensor.

A. Restrictions imposed by the spherical symmetry

The symmetry analysis of the integrals Eq. (12) becomes more straightforward when the spherical harmonics $\boldsymbol{W}$ are presented in a vector form. To this end we use the following relationship between the Cartesian basis vectors and the electric dipole harmonics in the limit $k \to 0$: $\boldsymbol{N}^{(1)}_{e11}(0,\mathbf{r}) \equiv \boldsymbol{N}_x \propto \boldsymbol{e}_x$, $\boldsymbol{N}^{(1)}_{o11}(0,\mathbf{r}) \equiv \boldsymbol{N}_y \propto \boldsymbol{e}_y$, $\boldsymbol{N}^{(1)}_{e01}(0,\mathbf{r}) \equiv \boldsymbol{N}_z \propto \boldsymbol{e}_z$. This allows us to rewrite the integral Eq. (12) as

$$I_{\mu n,\mu' n'\to\mu'' n''} \propto \chi^{(2)}_{\alpha\beta\gamma} \int_{r<a} \mathrm{d}V [\boldsymbol{N}_\alpha \cdot \boldsymbol{W}_{\mu n}(\boldsymbol{r})] \times [\boldsymbol{N}_\beta \cdot \boldsymbol{W}_{\mu' n'}(\boldsymbol{r})][\boldsymbol{N}_\gamma \cdot \boldsymbol{W}_{\mu'' n''}(\boldsymbol{r})]. \quad (13)$$

Let us consider the integral (13) in more detail. First of all, it contains a sum of several integrals of three scalar products of vector spherical harmonics, where each term corresponds to one of $\chi^{(2)}$-tensor components. We are seeking for the cases when the integrand is invariant under the transformations of the $O(3)$ symmetry group. We expect the integral to be nonzero, if at least one of the integrand terms contains a function invariant under all rotations and inversion transformation. The scalar products entering Eq. (13) can be readily expanded over the scalar spherical harmonics, see Refs. [44,45] and Appendix B. Afterwards, the resulting integrals can be analyzed for different $\chi^{(2)}$-tensor components and three general *rules A*, *B*, and *C*, governing whether the integrals are zero or not, can be formulated for each component separately.

Rule A: Parity under inversion and reflection in the $y = 0$ plane. The vector spherical harmonics (Appendix A) are transformed in the same way as the real scalar spherical harmonics $\psi_{\substack{e\\o}mn}$ [46–49] under the coordinate *rotations*, while under *inversion* $\psi_{\substack{e\\o}mn}$ and $\boldsymbol{N}_{\substack{e\\o}mn}$ acquire a sign $(-1)^n$ and $\boldsymbol{M}_{\substack{e\\o}mn}$ acquires a sign $(-1)^{n+1}$, so the parity of magnetic vector harmonics is inverse to the parity of electric and scalar harmonics. We introduce the *parity indices* $p_i = (-1)^n$ for $\boldsymbol{N}_{\substack{e\\o}mn}$, and $p_i = (-1)^{n+1}$ for $\boldsymbol{M}_{\substack{e\\o}mn}$ describing the behavior of spherical harmonics under the spatial inversion. Another parity index p_r describes the behavior of the harmonics under the reflection in the $y = 0$ plane, equivalent to the change of the azimuthal angle $\varphi \to -\varphi$. The functions ψ_{emn}, $\boldsymbol{N}_{emn}$, and $\boldsymbol{M}_{omn}$ are even with respect to such reflection, $p_r = 1$, while the functions ψ_{omn}, $\boldsymbol{N}_{omn}$, and $\boldsymbol{M}_{emn}$ are odd, $p_r = -1$. Thus, the inversion and reflection parity selection rules can be summarized as

$$p_i p_{i'} p_{i''} = -1 \text{ (inversion)}, \quad (14)$$

$$p_r^{\alpha\beta\gamma} p_r p_{r'} p_{r''} = 1 \text{ (reflection)}. \quad (15)$$

The rule Eq. (14) is applied to the right-hand side of Eq. (13) as a whole. The rule Eq. (15) is applied to the individual products of different Cartesian components corresponding to each nonzero element $\chi_{\alpha\beta\gamma}$ of the nonlinear susceptibility tensor in Eq. (13). The factor $p_r^{\alpha\beta\gamma}$ in Eq. (15) is the parity of the product $x_\alpha x_\beta x_\gamma$ under the reflection, which is illustrated in Fig. 10. In the following, we will also use notation of $p^{\omega}_{i(r)}$ or $p^{2\omega}_{i(r)}$ for the parity indices corresponding to the fundamental or the SH modes.

Rule B: Conservation of the angular momentum projection. Once the scalar products in Eq. (13) are calculated, the matrix element is reduced to the overlap integral of scalar spherical harmonics. The angular momentum projection rule for the tesseral harmonics can be written as

$$\pm m^\alpha \pm m^{2\omega} \pm m^\beta \pm m'^{\omega} \pm m^\gamma \pm m''^{\omega} = 0. \quad (16)$$

The matrix element (13) can be nonzero only if there exists a combination of signs when Eq. (16) is satisfied.

Rule C: Triangle inequality for the total angular momentum. This rule can be formulated as

$$-h + |n'^{\omega} - n''^{\omega}| \leqslant n^{2\omega} \leqslant |n'^{\omega} + n''^{\omega}| + h, \quad (17)$$

where the index $h \in [0..3]$ denotes the number of electric harmonics under the integral (12). The presence of the index h stems from the fact that the Cartesian components of vector

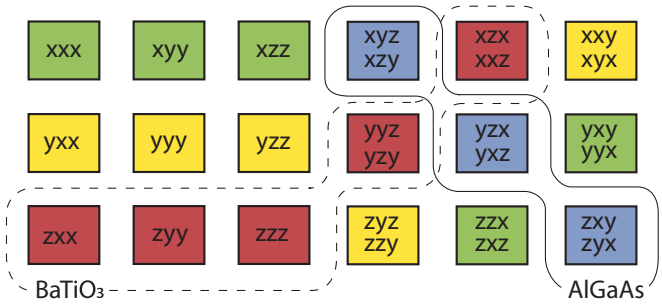

	$p_r^{\alpha\beta\gamma}$	$\pm m^\alpha \pm m^\beta \pm m^\gamma$
$BaTiO_3$	1	even
	-1	odd
	1	odd
AlGaAs	-1	even

FIG. 10. Parity indices of the $\hat{\chi}^{(2)}$-tensor components. The solid and dashed lines show the nonzero tensor components for AlGaAs and $BaTiO_3$ correspondingly for the crystal lattice oriented according to Fig. 1.

electric harmonics with the total angular momentum n include only the scalar harmonics with the momentum $n \pm 1$, while the projections of magnetic harmonics include only the states with the same angular momentum n.

Now, let us illustrate the rules obtained above with some specific examples. We start with examining the possibility of the generation of z-polarized electric dipolar mode ($\mathbf{N}_z = \mathbf{N}_{e01}$) in a AlGaAs nanoparticle by combining the y-polarized magnetic dipolar mode ($\mathbf{M}_y = \mathbf{M}_{o11}$) and the x-polarized electric dipolar mode ($\mathbf{N}_x = \mathbf{N}_{e11}$). Here $p_i p_{i'} p_{i''} = 1$, so such generation is prohibited by the first selection rule. Next, we try to replace $\mathbf{N}_z$ by some electric quadrupolar mode, for example, $\mathbf{N}_{o12}$. For this mode we have $p_i p_{i'} p_{i''} = -1$, $p_r^{\alpha\beta\gamma} = -1$ according to Fig. 10, and $p_r^{\alpha\beta\gamma} p_r p_{r'} p_{r''} = (-1) \cdot (-1) \cdot 1 \cdot 1 = 1$. Hence, such a process is not prohibited by the first two rules. But the sum of angular momentum projections (16) for considered three multipoles is always odd, while for the tensor component it is even (Fig. 10). This means that the total sum is never zero, and such a generation process is prohibited by the second rule.

These rules above provide a large number of possible cancellations, however, some exceptions are possible due to the properties of scalar products. To get all cancellations for the specific tensor component, we either should use the rules of how three scalar products are coupled, following the algorithm given in Appendix B, or apply additional symmetry reasons, discussed below.

B. Restrictions imposed by the crystal point group symmetry

In the previous Sec. III A, we have separately considered the cancellations of the terms in Eq. (12) corresponding to the individual components of the $\chi^{(2)}$ tensor. However, some of the components $\chi^{(2)}_{\alpha\beta\gamma}$ are equal due to the crystal point group symmetry that can result in additional cancellations after the summation over tensor components is performed. Such mutual cancellations are taken care of by the theory of representations of symmetry groups in a universal automatic fashion. The detailed analysis is given below.

a. Transformation of the matrix elements under symmetry operations. In order to determine the behavior of the matrix elements Eq. (12) under the application of the point symmetry group operation, we consider how vector spherical harmonics are transformed. Here, one has to take into account that the transformed harmonic is in general expressed via a sum of the harmonics with different angular momentum projections m and parity e/o, but the same polarization (M or N) and the same total angular momentum n [46–49]. The scalar products, entering the integral Eq. (13) are transformed under the symmetry operation $\boldsymbol{r} \to D^{(1)}\boldsymbol{r}$ as

$$\mathbf{N}_\alpha(D^{(1)}\mathbf{r}) \cdot \mathbf{W}_{\mu n}(D^{(1)}\boldsymbol{r}) = D^{(1)}_{\tilde{\alpha}\alpha} D^{(n)}_{\tilde{\mu}\mu} \mathbf{N}_{\tilde{\alpha}}(\mathbf{r}) \cdot \mathbf{W}_{\tilde{\mu}n}(\mathbf{r}). \quad (18)$$

Here $D^{(n)}_{\tilde{\mu}\mu}(g)$ are the representation matrices of the symmetry operation g with momentum n for tesseral harmonics [50], in case of rotations they reduce to the combinations of the Wigner matrices. As an example we consider the case when the $\mathbf{W}$ harmonics are the electric dipole harmonics, $\mathbf{W}_{\mu n} \to \mathbf{N}_\beta$, $\beta = x, y, z$ and $D^{(1)}$ is a rotation around the z axis, e.g., $D^{(1)}_{xx} = D^{(1)}_{yy} = \cos\varphi$, $D^{(1)}_{xy} = -D^{(1)}_{yx} = -\sin\varphi$, $D^{(1)}_{zz} = 1$. In this case Eq. (18) simplifies to

$$[\mathbf{N}_\alpha \cdot \mathbf{N}_\beta](D^{(1)}\mathbf{r}) = D^{(1)}_{\tilde{\alpha}\alpha} D^{(1)}_{\tilde{\beta}\beta} \mathbf{N}_{\tilde{\alpha}}(\mathbf{r}) \cdot \mathbf{N}_{\tilde{\beta}}(\mathbf{r}), \quad (19)$$

i.e., a scalar product of two electric dipole modes is transformed as a second-rank cartesian tensor.

The condition that the integral Eq. (13) remains invariant under the symmetry transformation Eq. (18) is written as

$$I_{\mu n,\mu' n' \to \mu'' n''} = D^{(n)}_{\tilde{\mu}\mu} D^{(n')}_{\tilde{\mu}'\mu'} D^{(n'')}_{\tilde{\mu}''\mu''} \widetilde{I}_{\tilde{\mu}n,\tilde{\mu}' n' \to \tilde{\mu}'' n''}, \quad (20)$$

where the matrix elements $\widetilde{I}$ are given by Eq. (12) with $\chi_{\alpha\beta\gamma}$ being replaced by

$$\widetilde{\chi}^{(2)}_{\alpha'\beta'\gamma'} = D^{(1)}_{\alpha\alpha'} D^{(1)}_{\beta\beta'} D^{(1)}_{\gamma\gamma'} \chi^{(2)}_{\alpha\beta\gamma}. \quad (21)$$

b. Application to harmonic generation. The most general consideration would require an expansion of the $\chi^{(2)}$ tensors Eq. (7), Eq. (8) of $BaTiO_3$ and AlGaAs, transforming under the spherical symmetry operations according to Eq. (21), over the irreducible representations of the $O(3)$ symmetry group. However, in practice it turns out that the relevant cancellations of the matrix elements Eq. (13), not captured in the previous Sec. III A, can be explained in a simpler way. Instead of the whole $O(3)$ group it suffices to apply a crystal point subgroup of the $O(3)$ group, i.e., to use a smaller set of symmetry operations. When the crystal point group operation is applied, the tensor $\chi^{(2)}$ stays invariant, which means that $\widetilde{\chi} = \chi$, and $\widetilde{I} = I$. Hence, the matrix elements I in Eq. (20) are transformed as a direct product of the three representations governing the transformation of the corresponding vector spherical harmonics. In order to stay nonzero, the integrals Eq. (20) should contain a combination, invariant to the symmetry operation of the crystal. More formally, the reducible representation governing the transformation Eq. (13) should contain an identity representation.

The symmetry analysis of the second harmonic generation is then reduced to (i) expanding the vector spherical

harmonics over the basis functions of the irreducible representation of the crystal point symmetry group and (ii) using the Clebsh-Gordan coefficients available for all point groups [42,51]. The classification of the dipole, quadrupole, and octupole spherical harmonics for T_d and C_{4v} point groups of AlGaAs and $BaTiO_3$, respectively, is given in Appendix C and Table VI. The examples of basis functions of irreducible representations, which behave in the same way under symmetry transformations as the spherical harmonics, are also given. The expansion has been done using the transformation properties of vector spherical harmonics.

For example, we see from Table VI that the electric dipole modes are transformed in the T_d group according to the F_2 irreducible representation, i.e., as components of the radius vector $\boldsymbol{r}$. Conversely, the magnetic dipole modes behave as pseudovector components, i.e., according to the F_1 representation.

Such an approach allows us to find all the selection rules of the nanoparticle with the same or higher symmetry as the material [Fig. 9(a)]. It can be a tetrahedral nanoparticle for T_d or a quadrangular pyramid nanoparticle for C_{4v}. This is possible due to the fact that we consider the integrand behavior under such transformations only. The further cancellations can appear due to the scalar product properties, for example, the z component of $\mathbf{M}_{e01}$ harmonic is zero, so it can provide some extra restrictions (see Appendix B).

IV. DISCUSSIONS

Let us apply the developed selection rules to the cases studied in Sec. II, where we already discussed the absence of particular harmonics in the generated field.

Plane-wave excitation. Under the excitation of $BaTiO_3$ (AlGaAs) nanoparticle with a plane wave, we observed the absence MD (ED) modes in the SH field. It is illustrative to start with the restrictions imposed by the spherical symmetry of modes that account for most of the selection rules.

Here, we will consider only the dipole terms in the excitation, and higher modes can be treated analogously. Applying Rule A to the $BaTiO_3$ nanoparticle in the case of dipole modes ($n = 1$) we do not obtain any restrictions due to the inversion parity, because both terms $ED \otimes ED$ and $MD \otimes ED$ are contained in the fundamental field. One can find that the reflection parity of the SH mode should be $p_r^{2\omega} = 1$. Indeed, according to the Mie theory generated dipole modes at the fundamental frequency can be only $\mathbf{N}_{e11}$ and $\mathbf{M}_{o11}$, and for both of them $p_r^{\omega} = 1$, while for $BaTiO_3$ $\hat{\chi}^{(2)}$ tensor $p_r^{\alpha\beta\gamma} = 1$ (see Fig. 10). From the angular momentum projection conservation Rule B, we find the limits for angular momentum of SH modes. For the tensor components the sum $\pm m^{\alpha} \pm m^{\beta} \pm m^{\gamma}$ is even according to Fig. 10. Thus, $\pm m^{2\omega} \pm m'^{\omega} \pm m''^{\omega}$ should also be even, and from the Mie theory it follows that $m'^{\omega} = m''^{\omega} = 1$, which makes $m^{2\omega}$ even. This immediately rules out all magnetic dipole modes as the only dipole mode with even m and $p_r^{2\omega} = 1$ is $\mathbf{M}_{o01}$, which is identical to zero. Electric dipole mode $\mathbf{N}_{e01}$ has the same reflection parity and, thus, is allowed in the SHG process (see Table III). These reasons also show that the higher order magnetic and electric modes can also exist. According to Rule C the highest possible harmonic generated from the dipole modes is the electric mode with $n = 5$ as shown in Table III: $ED \otimes ED \to ET$.

TABLE II. Single-mode excitation. Generated nonlinear multipoles in $BaTiO_3$ nanoparticle for two orientations of the pump MD moment under the rotation in the yz plane ($\varphi = \pi/2$). The shaded region coincides with the shaded region in Table III.

pump MD	SHG
$\theta = \pi/2$ (m_y)	ED, MQ, EO N_{e01}, M_{o22}, N_{e03}, N_{e23}
$\theta = 0$ (m_z)	ED, EO N_{e01}, N_{e03}

The selection rules for AlGaAs are shown in Table V. The same arguments as in the case of $BaTiO_3$ can be applied, while considering dipole channels of SHG. The only difference is that the parity of tensor components for AlGaAs $p_r^{\alpha\beta\gamma} = -1$ (see Fig. 10). Rule A will be fulfilled if the parity p_r of one of the modes will be changed in sign, allowing $MD \otimes ED \to MD$ transition. Other possible channels $ED \otimes ED \not\to ED$ or $MD \otimes MD \not\to ED$ are forbidden, as it would require generation of $\mathbf{N}_{o01}$ mode, which is identical to zero. Moreover, the dipole modes generation in SH field will be still prohibited even if the higher order modes will be excited at fundamental wavelength.

Single magnetic mode excitation. In Sec. II B, we have discussed the excitation of the SH mode with a single magnetic mode at the fundamental frequency. Let us first study in more detail the case of y-oriented dipole $\mathbf{M}_{o11}$. Applying derived selection rules, one can get from Rule C that the highest possible generated mode is the octupole mode $n \leqslant 3$. For $BaTiO_3$ nanoparticle from Rule B, we have already established that $m^{2\omega}$ should be even. The inversion and reflection parities from Rule A gives us that $p_i^{2\omega} = -1$ and $p_r^{2\omega} = 1$. For total angular momentum value of $n = 3$ this means that only electric modes should be generated (inversion rule), and they should be even (reflection rule), which gives us for even m only two possible modes: $\mathbf{N}_{e03}$ and $\mathbf{N}_{e23}$. For $n = 2$ only odd magnetic quadrupole mode possesses required reflection and inversion parity, which gives us only $\mathbf{M}_{o22}$ contribution as $\mathbf{M}_{o02} \equiv 0$. These selection rules are summarized in the highlighted row of Table II, which also corresponds to the highlighted region of the extended Table III.

Until now we have considered only one orientation of the crystalline lattice, shown in Fig. 1. However, the different orientation of the $BaTiO_3$ lattice provides other selection

TABLE III. Possible multipoles generated in second harmonic by the dipolar terms products in the incident field. $BaTiO_3$ lattice orientation is $[100]\|\mathbf{e}_x$, $[010]\|\mathbf{e}_y$, $[001]\|\mathbf{e}_z$.

Incident field	SH								
	Magnetic				Electric				
	D	Q	O	H	D	Q	O	H	T
$N_{e11} \otimes N_{e11}$ $p_x \otimes p_x$		M_{o22}		M_{o24}	N_{e01} (p_z)		N_{e03} N_{e23}		N_{e05} N_{e25}
$M_{o11} \otimes M_{o11}$ $m_y \otimes m_y$		M_{o22}			N_{e01} (p_z)		N_{e03} N_{e23}		
$M_{o11} \otimes N_{e11}$ $m_y \otimes p_x$			M_{o23}			N_{e02} N_{e22}		N_{e04} N_{e24}	

TABLE IV. Possible multipoles generated in second harmonic by the dipolar terms products in the incident field. $BaTiO_3$ lattice orientation is $[100]\|\mathbf{e}_y$, $[010]\|\mathbf{e}_z$, $[001]\|\mathbf{e}_x$

Incident field	SH								
	Magnetic				Electric				
	D	Q	O	H	D	Q	O	H	T
$N_{e11}\otimes N_{e11}$ $p_x\otimes p_x$					N_{e11} (p_x)		N_{e13} N_{e33}		N_{e15} N_{e35}
$M_{o11}\otimes M_{o11}$ $m_y\otimes m_y$		M_{o12}			N_{e11} (p_x)		N_{e13} N_{e33}		
$M_{o11}\otimes N_{e11}$ $m_y\otimes p_x$	M_{o11} (m_y)		M_{o13} M_{o33}			N_{e12}		N_{e14} N_{e34}	

rules. For instance, one can rotate the $BaTiO_3$ lattice by 90° obtaining $[100]\|\mathbf{e}_y$, $[010]\|\mathbf{e}_z$, $[001]\|\mathbf{e}_x$, which changes the parity indices $p_r^{\alpha\beta\gamma}=1$, and $\pm m^\alpha \pm m^\beta \pm m^\gamma$ should be odd. The resulting selection rules are summarized in Table IV. One can see that harmonics with different projection m can be generated, allowing both MD and ED channels. This provides us an opportunity to control the SH signal by changing the relative orientation between the field polarization and the crystalline lattice.

The same approach allows us to analyze the modes generated at SH by pumping at single MD mode in the AlGaAs nanoparticle, as shown in Table I. The shaded region describes excitation of the MD mode corresponding to y-oriented magnetic dipole (m_y). The same argument as in the case of $BaTiO_3$ allows up to octupole mode generation. We have already discussed in this section that the generation of ED mode is possible in AlGaAs due to the $p_r^{\alpha\beta\gamma}=-1$ parity. Because of that, the inversion and reflection parity values should be equal to $p_i^{2\omega}=-1$ and $p_r^{2\omega}=-1$. Thus, for $n=3$ $\mathbf{N}_{o23}$ is the only nonzero mode satisfying the parity conditions, while for $n=2$ the even magnetic modes have proper parity, thus, $\mathbf{M}_{e02}$ and $\mathbf{M}_{e22}$ are present (shaded rows in Tables I and V).

The selection rules provided by the crystalline lattice symmetry. So far we have discussed the selection rules which were governed by the symmetry of the vector spherical harmonics and related conditions *A, B,* and *C*. However, there are SHG channels, which are allowed by the mode symmetry but become restricted due to crystalline symmetry only.

For the SHG by rotated MD in AlGaAs nanoparticle for $\varphi=\pi/4$ (see Table I) modes $\mathbf{M}_{o11}$ and $\mathbf{M}_{e11}$ are present in the fundamental field, while the channels of generation

TABLE V. Possible multipoles generated in the second harmonic by the dipolar terms products in the incident field. AlGaAs lattice rotation angle is $\beta=0°$.

Incident field	SH								
	Magnetic				Electric				
	D	Q	O	H	D	Q	O	H	T
$N_{e11}\otimes N_{e11}$ $p_x\otimes p_x$		M_{e02} M_{e22}		M_{e04} M_{e24} M_{e44}			N_{o23}		N_{o25} N_{o45}
$M_{o11}\otimes M_{o11}$ $m_y\otimes m_y$		M_{e02} M_{e22}					N_{o23}		
$M_{o11}\otimes N_{e11}$ $m_y\otimes p_x$	M_{e01} (m_z)		M_{e03} M_{e23}			N_{o22}		N_{o24} N_{o44}	

TABLE VI. Symmetry classification of vector spherical harmonics.

Spherical Harmonic		AlGaAs (T_d)		$BaTiO_3$ (C_{4v})	
ED	$\boldsymbol{N}_{o11}$	F_2	y	E	y
	$\boldsymbol{N}_{e11}$		x		x
	$\boldsymbol{N}_{e01}$		z	A_1	z
MD	$\boldsymbol{M}_{o11}$	F_1	L_y	E	x or L_y
	$\boldsymbol{M}_{e11}$		L_x		y or L_x
	$\boldsymbol{M}_{e01}$		L_z	A_2	L_z
EQ	$\boldsymbol{N}_{o12}$	F_2	x	E	y
	$\boldsymbol{N}_{e12}$		y		x
	$\boldsymbol{N}_{o22}$		$2z$	B_2	xy
	$\boldsymbol{N}_{e22}$	E	$6(x^2-y^2)$	B_1	x^2-y^2
	$\boldsymbol{N}_{e02}$		$2z^2-x^2-y^2$	A_1	z
MQ	$\boldsymbol{M}_{o12}$	F_1	L_x	E	x or L_y
	$\boldsymbol{M}_{e12}$		L_y		y or L_x
	$\boldsymbol{M}_{o22}$		L_z	B_1	x^2-y^2
	$\boldsymbol{M}_{e22}$	E	$2z^2-x^2-y^2$	B_2	xy
	$\boldsymbol{M}_{e02}$		$6(x^2-y^2)$	A_2	L_z
EO	$\boldsymbol{N}_{o13}$	F_2+F_1	$-6y+L_y$	E	y
	$\boldsymbol{N}_{e13}$		$-6x-L_x$		x
	$\boldsymbol{N}_{o23}$	A_1	1 or xyz	B_2	xy
	$\boldsymbol{N}_{e23}$	F_1	$4L_z$	B_1	x^2-y^2
	$\boldsymbol{N}_{o33}$	F_1+F_2	$-60y-6L_y$	E	y
	$\boldsymbol{N}_{e33}$		$60x-6L_x$		x
	$\boldsymbol{N}_{e03}$	F_2	$4z$	A_1	z
MO	$\boldsymbol{M}_{o13}$	F_2+F_1	$-6L_y+y$	E	L_y
	$\boldsymbol{M}_{e13}$		$-6L_x-x$		L_x
	$\boldsymbol{M}_{o23}$	A_2	$1*$ or $L_xL_yL_z$	B_1	x^2-y^2
	$\boldsymbol{M}_{e23}$	F_2	$4z$	B_2	xy
	$\boldsymbol{M}_{o33}$	F_1+F_2	$-60L_y-6y$	E	L_y
	$\boldsymbol{M}_{e33}$		$60L_x-6x$		L_x
	$\boldsymbol{M}_{e03}$	F_1	$4L_z$	A_2	L_z

of higher quadrupole modes are forbidden $\mathbf{M}_{o11}\otimes\mathbf{M}_{e11}\not\to \mathbf{M}_{o12}, \boldsymbol{M}_{e12}, \boldsymbol{M}_{o22}$, however some of them satisfy the mode symmetry rules. These processes are restricted by the crystalline symmetry rules discussed in Sec. III B: In the T_d symmetry group the magnetic dipole modes are transformed as components of the pseudovector $\boldsymbol{L}$ (F_1 representation). The modes $\boldsymbol{M}_{o12}$, $\boldsymbol{M}_{e12}$, $\boldsymbol{M}_{o22}$ also behave under the symmetry operations as components of a pseudovector $\boldsymbol{L}$ (F_1 representation), see Table VI. Now, the physical question, of whether the SHG process is possible, is reduced to the mathematical question of whether the direct product $F_1\otimes F_1$ contains F_1. The nine-dimensional reducible representation $F_1\otimes F_1$ is equal to a direct sum of irreducible representations $A_1\oplus E\oplus F_2\oplus F_1$ [42,51]. If we label the 3-pseudovectors, forming the basis of the representation $\boldsymbol{F}_1$ as $\boldsymbol{M}$ and $\boldsymbol{M}'$, the nine linear combinations transforming to A_1, E, F_1, F_2 are $\boldsymbol{M}\cdot\boldsymbol{M}'$ (A_1), $\sqrt{3}(\mathbf{M}_x\mathbf{M}'_x-\mathbf{M}_y\mathbf{M}'_y)$ and $2\mathbf{M}_z\mathbf{M}'_z-\mathbf{M}_x\mathbf{M}'_x-\mathbf{M}_y\mathbf{M}'_y$ (E), $\mathbf{M}_x\mathbf{M}'_y+\mathbf{M}_y\mathbf{M}'_x$ and two cyclic permutations (F_2) and $\boldsymbol{M}\times\boldsymbol{M}'$ (F_1). The latter must be understood componentwise. We are interested only in the magnetic dipole

contribution, i.e., in the pseudovector $\boldsymbol{M} \times \boldsymbol{M}'$ transforming according to F_1. However, in our case $\boldsymbol{M}$ and $\boldsymbol{M}'$ are equal, since both modes at the first harmonic frequency belong to the same electric field. As such, the vector product $\boldsymbol{M} \times \boldsymbol{M}'$ is zero and the conversion from the magnetic dipole modes to the $\boldsymbol{M}_{o12}, \boldsymbol{M}_{e12}, \boldsymbol{M}_{o22}$ quadrupolar modes is forbidden by the T_d crystal symmetry. For similar reasons, such a process is prohibited for the conversion from the electric dipole modes $\mathbf{N}_{o11}$ and $\mathbf{N}_{e11}$. On the other hand, a sum frequency generation process, when the incident modes have different frequency, can be possible, since $\boldsymbol{M} \times \boldsymbol{M}'$ in general is not zero.

Anisotropy of the linear response of the nanoparticle. Finally, let us briefly discuss the effect of the uniaxial symmetry of the linear response of the dielectric tensor, present for $BaTiO_3$ on the obtained selection rules for the second harmonic generation. The impact of anisotropy on linear scattering has been studied in details in Refs. [52,53]. However, for the considered range of parameters the anisotropy is not very strong, namely $\sqrt{\varepsilon_{xx}} = \sqrt{\varepsilon_{yy}} = 2.33$ and $\sqrt{\varepsilon_{zz}} = 2.29$ at the fundamental wavelength of 1050 nm [54] and $\sqrt{\varepsilon_{xx}} = \sqrt{\varepsilon_{yy}} = 2.48$ and $\sqrt{\varepsilon_{zz}} = 2.42$ at the SH wavelength of 525 nm [55], a rigorous extension of the approach presented in this paper to the anisotropic case manifests itself a complicated problem. Thus, we have applied numerical simulation method in order to check the effects of the present material anisotropy on the SH field multipole content. The spectral dependence of the SHG cross section is shown in Fig. 11 similarly to Fig. 2 but with account for anisotropic permittivity tensor. Simulations results have shown that the difference in the nonlinear response is rather weak, and the multipolar contents are generally preserved for the given set of the parameters.

The further speculations on the influence of the anisotropy will bring us to the conclusion on the selection rules modification. In general, the linear scattering of a plane wave on an isotropic particle preserves both the multipole order (n, m), and the electric or magnetic parity, namely each spherical harmonic contained in a plane wave generates a scattered harmonic with the same numbers (n, m), and the same electric/magnetic parity. In the process of anisotropic particle scattering the mode numbers are not conserved [53,56] and multipole orders n, their projections m (in case of arbitrary orientation of the optic axis of the crystal), and electric and magnetic degrees of freedom are getting mixed. The SHG process will also entangle the multipole orders due to the structure of the anisotropic Green's function. These two processes change the selection rules A–C. However, the formulation of the exact selection rules in this case is a matter of future work; there will be a particular resemblance to the case of the SHG from a cylindrical nanoparticle with isotropic linear permittivity tensor [57].

V. CONCLUSION

In conclusion, we have theoretically analyzed the second harmonic generation by spherical dielectric nanoparticles made of materials with nonzero bulk second order nonlinear susceptibility tensor $\hat{\chi}^{(2)}$. Considering two typical crystalline solids, $BaTiO_3$ and AlGaAs, we have studied the intensity of SHG under a plane wave illumination and analyzed the contribution of different multipole components into the total SH intensity. We have shown that under the resonant excitation of a single magnetic dipole mode one can achieve control of the directionality of SH emission by rotating the dipole moment with respect to the material's crystalline lattice. Finally, we have developed a symmetry approach which provides an explanation why only particular modes can be observed in the SH field and defined general selection rules for SHG. Our symmetry analysis fully agrees with numerical and analytical results and also demonstrates promising predictive power, which can be used for design of efficient nonlinear light sources based on nanoparticle ensembles.

ACKNOWLEDGMENTS

The authors acknowledge useful discussions with S. E. Derkachev, A. A. Nikolaeva, M. O. Nestoklon, E. L. Ivchenko, and A. I. Smirnov. The work was supported by the Russian Foundation for Basic Research (Grants No. 18-02-00381, No. 18-02-01206, No. 18-32-20065, and No. 16-02-00684). Numerical modeling, performed by D.S., was supported by the Russian Science Foundation (Grant No. 17-12-01574). A.P. and M.P. have been supported by the Foundation for the Advancement of Theoretical Physics and Mathematics "Basis."

APPENDIX A: VECTOR SPHERICAL HARMONICS

Vector spherical harmonics used above are defined as

$$\mathbf{M}_{\substack{e\\o}mn} = \nabla \times \left(\mathbf{r}\psi_{\substack{e\\o}mn}\right), \tag{A1}$$

$$\mathbf{N}_{\substack{e\\o}mn} = \frac{\nabla \times \mathbf{M}_{\substack{e\\o}mn}}{k}, \tag{A2}$$

where

$$\psi_{emn} = \cos m\varphi P_n^m(\cos\theta) z_n(\rho), \tag{A3}$$

$$\psi_{omn} = \sin m\varphi P_n^m(\cos\theta) z_n(\rho) \tag{A4}$$

are the scalar spherical functions, proportional to the tesseral spherical functions. Functions $z_n(\rho)$ can be replaced by spherical Bessel functions of any type, ρ is $k(\omega)r = \omega\sqrt{\varepsilon}r/c$.

$$\mathbf{M}_{emn}(k, \mathbf{r}) = \frac{-m}{\sin(\theta)} \sin(m\varphi) P_n^m(\cos(\theta)) z_n(\rho)\mathbf{e}_\theta - \cos(m\varphi)\frac{dP_n^m(\cos(\theta))}{d\theta} z_n(\rho)\mathbf{e}_\varphi, \tag{A5}$$

$$\mathbf{M}_{omn}(k, \mathbf{r}) = \frac{m}{\sin(\theta)} \cos(m\varphi) P_n^m(\cos(\theta)) z_n(\rho)\mathbf{e}_\theta - \sin(m\varphi)\frac{dP_n^m(\cos(\theta))}{d\theta} z_n(\rho)\mathbf{e}_\varphi, \tag{A6}$$

$$\mathbf{N}_{emn}(k, \mathbf{r}) = \frac{z_n(\rho)}{\rho} \cos(m\varphi) n(n+1) P_n^m(\cos(\theta))\mathbf{e}_\mathbf{r} + \cos(m\varphi)\frac{dP_n^m(\cos(\theta))}{d\theta}\frac{1}{\rho}\frac{d}{d\rho}[\rho z_n(\rho)]\mathbf{e}_\theta - m\sin(m\varphi)\frac{P_n^m(\cos(\theta))}{\sin(\theta)}\frac{1}{\rho}\frac{d}{d\rho}[\rho z_n(\rho)]\mathbf{e}_\varphi, \tag{A7}$$

$$\mathbf{N}_{omn}(k,\mathbf{r}) = \frac{z_n(\rho)}{\rho}\sin(m\varphi)n(n+1)P_n^m(\cos(\theta))\mathbf{e}_\mathbf{r} + \sin(m\varphi)\frac{dP_n^m(\cos(\theta))}{d\theta}\frac{1}{\rho}\frac{d}{d\rho}[\rho z_n(\rho)]\mathbf{e}_\theta + m\cos(m\varphi)\frac{P_n^m(\cos(\theta))}{\sin(\theta)}\frac{1}{\rho}\frac{d}{d\rho}[\rho z_n(\rho)]\mathbf{e}_\varphi. \tag{A8}$$

The Mie coefficients for the field inside the nanoparticle can be expressed as follows:

$$c_n(\omega) = \frac{[\rho_1 h_n(\rho_1)]' j_n(\rho_1) - [\rho_1 j_n(\rho_1)]' h_n(\rho_1)}{[\rho_1 h_n(\rho_1)]' j_n(\rho_2) - [\rho_2 j_n(\rho_2)]' h_n(\rho_1)} \tag{A9}$$

$$d_n(\omega) = \frac{\sqrt{\varepsilon_2}[\rho_1 h_n(\rho_1)]' j_n(\rho_1) - \sqrt{\varepsilon_2}[\rho_1 j_n(\rho_1)]' h_n(\rho_1)}{\varepsilon_2[\rho_1 h_n(\rho_1)]' j_n(\rho_2) - [\rho_2 j_n(\rho_2)]' h_n(\rho_1)}, \tag{A10}$$

here ρ_1 is $k_1(\omega)a = \omega\sqrt{\varepsilon_1}a/c$, ρ_2 is $k_2(\omega)a = \omega\sqrt{\varepsilon_2}a/c$.

The Green function for a dielectric sphere of radius a for $r > a > r'$ at frequency 2ω is given by

$$\widehat{\mathbf{G}}(\mathbf{r},\mathbf{r}',2\omega) = \frac{ik_2(2\omega)}{4\pi}\sum_{n=1}^{\infty}\sum_{m=0}^{n}(2-\delta_0)\frac{2n+1}{n(n+1)}\frac{(n-m)!}{(n+m)!} \cdot \left(a_n^{(2)}(2\omega)\left(\mathbf{M}_{emn}^{(3)}[k_1(2\omega),\mathbf{r}]\otimes\mathbf{M}_{emn}^{(1)}[k_2(2\omega),\mathbf{r}'] + \mathbf{M}_{omn}^{(3)}[k_1(2\omega),\mathbf{r}]\otimes\mathbf{M}_{omn}^{(1)}[k_2(2\omega),\mathbf{r}']\right) + b_n^{(2)}(2\omega)\left(\mathbf{N}_{emn}^{(3)}[k_1(2\omega),\mathbf{r}]\otimes\mathbf{N}_{emn}^{(1)}[k_2(2\omega),\mathbf{r}'] + \mathbf{N}_{omn}^{(3)}[k_1(2\omega),\mathbf{r}]\otimes\mathbf{N}_{omn}^{(1)}[k_2(2\omega),\mathbf{r}']\right)\right), \tag{A11}$$

where superscripts (1) and (3) appear, when we replace $z_n(\rho)$ by spherical Bessel functions, and the spherical Hankel functions of the first kind, respectively, $\delta_0 = 1$ when $m = 0$, and $\delta_0 = 0$ when $m \neq 0$. Coefficients in the Green function have a similar denominator as the Mie coefficients:

$$a_n^{(2)}(\omega) = \frac{[\rho_2 j_n(\rho_2)]' h_n(\rho_2) - [\rho_2 h_n(\rho_2)]' j_n(\rho_2)}{[\rho_2 j_n(\rho_2)]' h_n(\rho_1) - \mu_2/\mu_1[\rho_1 h_n(\rho_1)]' j_n(\rho_2)},$$

$$b_n^{(2)}(\omega) = \frac{[\rho_2 j_n(\rho_2)]' h_n(\rho_2) - [\rho_2 h_n(\rho_2)]' j_n(\rho_2)}{\mu_2/(\sqrt{\varepsilon}_2\mu_1)[\rho_2 j_n(\rho_2)]' h_n(\rho_1) - \sqrt{\varepsilon}_2[\rho_1 h_n(\rho_1)]' j_n(\rho_2)}.$$

The rigorous expression for the D-coefficients is as follows:

$$D_{W_{\substack{e\\o}mn}} = \left(\frac{2\omega}{c}\right)^2\frac{ik_2(2\omega)}{4\pi}(2-\delta_0)\frac{2n+1}{n(n+1)}\frac{(n-m)!}{(n+m)!}\begin{pmatrix}a_n^{(2)}(2\omega)\\ b_n^{(2)}(2\omega)\end{pmatrix}\int_V \mathbf{W}_{\substack{e\\o}mn}^{(1)}(k_2(2\omega),\mathbf{r})\widehat{\chi}\mathbf{E}^{\omega}(\mathbf{r})\mathbf{E}^{\omega}(\mathbf{r})dV\ .$$

Here, $\mathbf{W}_{\substack{e\\o}mn}^{(1)}(k_2(2\omega),\mathbf{r})$ is a vector spherical harmonic $\mathbf{M}_{\substack{e\\o}mn}^{(1)}(k_2(2\omega),\mathbf{r})$ or $\mathbf{N}_{\substack{e\\o}mn}^{(1)}(k_2(2\omega),\mathbf{r})$.

APPENDIX B: RIGOROUS APPROACH FOR THE SELECTION RULES IMPOSED BY THE SPHERICAL SYMMETRY

Considering three scalar products of vector spherical harmonics in Eq. (13), we find that each of them can be expanded in a finite sum of several specific scalar functions $\psi_{\substack{e\\o}mn}$ with the coefficients independent on angle [44,45]. In turn, the product of three scalar functions can be again represented in the form of a sum over spherical scalar harmonics. We are looking for the cases when the coefficient before the invariant term ψ_{e00} is nonzero, which also provides integral (13) is nonzero.

Here, we are only interested in the scalar products with Cartesian harmonics $\mathbf{N}_\alpha$, which have angular momentum $n = 1$. As a result, we have two different types of scalar products:

(1) If $\boldsymbol{W}_{\mu n}$ is replaced by $\mathbf{N}_{p_r mn}$, and $\mathbf{N}_\alpha$ is replaced by $\mathbf{N}_{p'_r m'1}$, where p_r is the parity index, introduced in Sec. III A, obtaining [58]:

$$[\mathbf{N}_{p'm'1}\mathbf{N}_{pmn}] \propto \sum_{\substack{m''=m\pm m',\\ n''=n\pm 1,\\ n''\neq n}} c(r)\psi_{p\cdot p'm''n''}. \tag{B1}$$

For instance:

$$[\mathbf{N}_{e01}(0,\mathbf{r})\cdot\mathbf{N}_{e01}(k,\mathbf{r}))] = [\mathbf{N}_{e01}]_z \tag{B2}$$

$$= \frac{2}{3}\left(\frac{z_1(\rho)}{\rho}\left(\frac{\psi_{e00}}{z_0(\rho)} + \frac{\psi_{e02}}{z_2(\rho)}\right) + \frac{z_0(\rho)-z_2(\rho)}{3}\left(\frac{\psi_{e00}}{z_0(\rho)} - \frac{\psi_{e02}}{z_2(\rho)}\right)\right). \tag{B3}$$

(2) If $\boldsymbol{W}_{\mu n}$ is replaced by $\mathbf{M}_{p_r mn}$, and $\mathbf{N}_\alpha$ is replaced by $\mathbf{N}_{p'_r m'1}$, we obtain a similar expression. Since for Cartesian projections of magnetic harmonics $n'' = n$, the summation over full angular momentum is simplified:

$$[\mathbf{N}_{p'm'1}\mathbf{M}_{pmn}] \propto \sum_{\substack{m''=m\pm m',\\ n''=n}} c(r)\psi_{p\cdot p'm''n''}. \tag{B4}$$

For instance:

$$[\mathbf{N}_{o11}(0,\mathbf{r})\cdot\mathbf{M}_{o11}(k,\mathbf{r})] = [\mathbf{M}_{o11}]_y \sim \psi_{o01} = 0 \tag{B5}$$

$$[\mathbf{N}_{e01}(0,\mathbf{r})\cdot\mathbf{M}_{e13}(k,\mathbf{r})] = [\mathbf{M}_{e13}]_z = \frac{2}{3}z_3(\rho)\psi_{o13} \tag{B6}$$

In our considerations, we are not interested in the exact form of the coefficients $c(r)$, because they have no angular dependence, so they are invariant under all transformations of the sphere and can't alter the selection rules. If radial

integration turns into zero, this is not due to the symmetry and can't be considered in this simple way. Finally, we obtain the integrand consisting of the sum of products of *scalar* spherical harmonics $\psi_{\substack{e\\o}mn}$, which can be easily expressed via the Clebsh-Gordan coefficients [49,59]. This means that the product of two of three scalar harmonics must contain a third one:

$$\psi_{p'm'n'}\psi_{pmn} \propto \sum_{m''=m\pm m',n''} \psi_{p\cdot p'm''n''} C^{n''0}_{n0n'0}. \tag{B7}$$

The Clebsh-Gordan coefficient $C^{n''0}_{n0n'0}$ is nonzero only when n'' has the same parity as sum of n and n'. The usual triangle inequality for n must be satisfied as well. It appears in accordance with the fact that the product of two functions should have the same inversion behavior as the third.

Below we present several examples of computation of the integrals, obtaining selection rules for particular mode channels:

$$\int_V \chi_{xxz}[\mathbf{N}_x\mathbf{M}_{o11}(2\omega)][\mathbf{N}_x\mathbf{M}_{o11}(\omega)][\mathbf{N}_z\mathbf{N}_{e01}(\omega)]dV \tag{B8}$$

$$= \int_V \chi_{xxz}[\mathbf{N}_{e11}(0)\mathbf{M}_{o11}(2\omega)][\mathbf{N}_{e11}(0)\mathbf{M}_{o11}(\omega)] \times [\mathbf{N}_{e01}(0)\mathbf{N}_{e01}(\omega)]dV \tag{B9}$$

$$\to \chi_{xxz}\int_V \psi_{e01}\psi_{e01}(c_1\psi_{e02} + c_2\psi_{e00})dV \neq 0, \tag{B10}$$

here c_1 and c_2 depend on the radius only and are angular independent. Thus, the coupling is possible with the tensor component χ_{xxz}.

$$\int_V \chi_{xxz}[\mathbf{N}_x(0)\mathbf{N}_{e11}(2\omega)][\mathbf{N}_x(0)\mathbf{M}_{o11}(\omega)][\mathbf{N}_z(0)\mathbf{N}_{e01}(\omega)]dV \tag{B11}$$

$$= \int_V \chi_{xxz}[\mathbf{N}_{e11}(0)\mathbf{N}_{e11}(2\omega)][\mathbf{N}_{e11}(0)\mathbf{M}_{o11}(\omega)] \times [\mathbf{N}_{e01}(0)\mathbf{N}_{e01}(\omega)]dV \tag{B12}$$

$$\to \chi_{xxz}\int_V (c_1\psi_{e22} + c_2\psi_{e00} + c_3\psi_{e02})\psi_{e01}\psi_{e02}dV = 0, \tag{B13}$$

so this coupling is prohibited because C^{20}_{1020} is zero. We see that actually, it is prohibited due to Rule A because the integrand is odd with respect to spatial inversion. The three selection Rules A–C, given in the main text, follow from this procedure, but mix all the harmonics, neglecting properties of specific scalar products.

APPENDIX C: SYMMETRY CLASSIFICATION OF VECTOR SPHERICAL HARMONICS

In order to reveal how the crystalline symmetry affects the possibility of multipolar generation, we need to know the behavior of the vector spherical functions under the transformations from the crystal symmetry group. Here we give the table for two types of crystalline symmetries where we indicate the corresponding irreducible representations and express the spherical functions via the basis functions of these representations, that are transformed via each other in the same way. The numerical coefficients are obtained properly, but their explicit values are not required to derive the selection rules. While the selection rules in spherical $BaTiO_3$ nanoparticles can be determined just from the conservation of the angular momentum projection quantum number m, the table can be also useful for the nanoparticles of the pyramidal shape. Similar classifications for other symmetries can be found in Ref. [60].

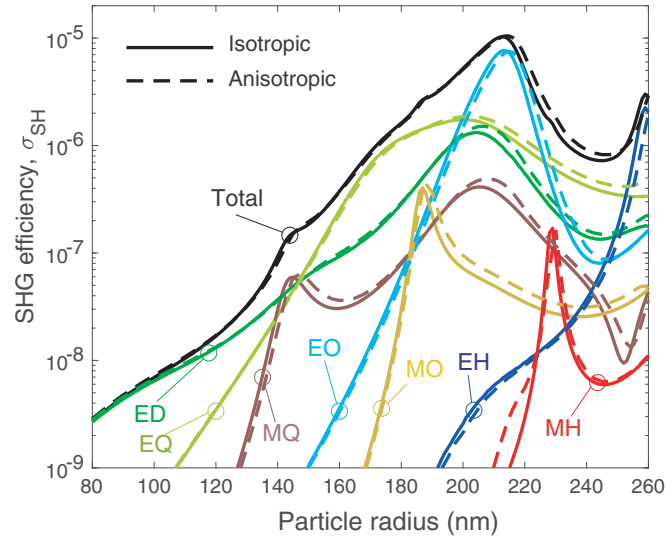

FIG. 11. The SHG cross section for $BaTiO_3$ nanoparticle without (solid lines) and with (dashed lines) account for the anisotropy of material parameters. All the parameters of simulations are the same as in Fig. 2(a), but the anisotropic tensor of the dielectric permittivity is defined by components $\sqrt{\varepsilon_{xx}} = \sqrt{\varepsilon_{yy}} = 2.48$ and $\sqrt{\varepsilon_{zz}} = 2.42$ at the SH wavelength of 525 nm.

APPENDIX D: ANISOTROPY OF THE LINEAR MATERIAL PARAMETERS

Here we provide the comparison between the SHG from a nanoparticle with isotropic and anysotropic tensor of dielectric permittivities as discussed in Sec. IV. The results of the numerical simulations of the SHG efficiency are presented in Fig. 11 for the case of a $BaTiO_3$ nanoparticle. The contributions coming from different multipole moments are shown with different colors and are marked. One can see that there is weak dependence of the obtained spectra for the given parameters of anisotropy.

[1] M. Kauranen and A. V. Zayats, Nonlinear plasmonics, Nat. Photonics **6**, 737 (2012).

[2] N. C. Panoiu, W. E. I. Sha, D. Y. Lei, and G.-C. Li, Nonlinear optics in plasmonic nanostructures, J. Opt. **20**, 083001 (2018).

[3] J. Butet, P.-F. Brevet, and O. J. F. Martin, Optical second harmonic generation in plasmonic nanostructures: From fundamental principles to advanced applications, ACS Nano **9**, 10545 (2015).

[4] R. W. Boyd, *Nonlinear Optics*, 3rd ed. (Academic Press, Burlington, 2003), pp. 69–133.

[5] A. Capretti, C. Forestiere, L. Dal Negro, and G. Miano, Full-wave analytical solution of second-harmonic generation in metal nanospheres, Plasmonics **9**, 151 (2014).

[6] A. I. Kuznetsov, A. E. Miroshnichenko, M. L. Brongersma, Y. S. Kivshar, and B. Luk'yanchuk, Optically resonant dielectric nanostructures, Science **354**, aag2472 (2016).

[7] D. A. Smirnova and Y. S. Kivshar, Multipolar nonlinear nanophotonics, Optica **3**, 1241 (2016).

[8] S. Kruk and Y. Kivshar, Functional meta-optics and nanophotonics governed by Mie resonances, ACS Photonics **4**, 2638 (2017).

[9] R. Camacho-Morales, M. Rahmani, S. Kruk, L. Wang, L. Xu, D. A. Smirnova, A. S. Solntsev, A. Miroshnichenko, H. H. Tan, F. Karouta, S. Naureen, K. Vora, L. Carletti, C. De Angelis, C. Jagadish, Y. S. Kivshar, and D. N. Neshev, Nonlinear generation of vector beams from AlGaAs nanoantennas, Nano Lett. **16**, 7191 (2016).

[10] J. Cambiasso, G. Grinblat, Y. Li, A. Rakovich, E. Cortés, and S. A. Maier, Bridging the gap between dielectric nanophotonics and the visible regime with effectively lossless GaP antennas, Nano Lett. **17**, 1219 (2017).

[11] P. P. Vabishchevich, S. Liu, M. B. Sinclair, G. A. Keeler, G. M. Peake, and I. Brener, Enhanced second-harmonic generation using broken symmetry III-V semiconductor fano metasurfaces, ACS Photonics **5**, 1685 (2018)

[12] V. F. Gili, L. Ghirardini, D. Rocco, G. Marino, I. Favero, I. Roland, G. Pellegrini, L. Duò, M. Finazzi, L. Carletti, A. Locatelli, A. Lemaître, D. Neshev, C. De Angelis, G. Leo, and M. Celebrano, Metal–dielectric hybrid nanoantennas for efficient frequency conversion at the anapole mode, Beilstein J. Nanotechnology **9**, 2306 (2018).

[13] D. Rocco, V. F. Gili, L. Ghirardini, L. Carletti, I. Favero, A. Locatelli, G. Marino, D. N. Neshev, M. Celebrano, M. Finazzi, G. Leo, and C. De Angelis, Tuning the second-harmonic generation in AlGaAs nanodimers via nonradiative state optimization [Invited], Photonics Research **6**, B6 (2018).

[14] L. Carletti, A. Locatelli, O. Stepanenko, G. Leo, and C. De Angelis, Enhanced second-harmonic generation from magnetic resonance in AlGaAs nanoantennas., Opt. Exp. **23**, 26544 (2015).

[15] A. N. Poddubny and D. A. Smirnova, Nonlinear generation of quantum-entangled photons from high-Q states in dielectric nanoparticles, arXiv:1808.04811.

[16] J. I. Dadap, J. Shan, and T. F. Heinz, Theory of optical second-harmonic generation from a sphere of centrosymmetric material: small-particle limit, J. Opt. Soc. Am. B **21**, 1328 (2004).

[17] Y. Pavlyukh and W. Hübner, Nonlinear mie scattering from spherical particles, Phys. Rev. B **70**, 245434 (2004).

[18] R. Singla and W. L. Mochan, arXiv:1901.00918.

[19] M. Finazzi, P. Biagioni, M. Celebrano, and L. Duò, Selection rules for second-harmonic generation in nanoparticles, Phys. Rev. B **76**, 125414 (2007).

[20] S. V. Makarov, M. I. Petrov, U. Zywietz, V. A. Milichko, D. A. Zuev, N. Y. Lopanitsyna, A. Y. Kuksin, I. S. Mukhin, G. P. Zograf, E. V. Ubyivovk, D. A. Smirnova, S. V. Starikov, B. N. Chichkov, and Y. S. Kivshar, Efficient second-harmonic generation in nanocrystalline silicon nanoparticles, Nano Lett. **17**, 3047 (2017).

[21] D. A. Smirnova, A. I. Smirnov, and Y. S. Kivshar, Multipolar second-harmonic generation by Mie-resonant dielectric nanoparticles, Phys. Rev. A **97**, 013807 (2018).

[22] S. S. Kruk, R. Camacho-Morales, L. Xu, M. Rahmani, D. Smirnova, L. Wang, H. H. Tan, C. Jagadish, D. N. Neshev, and Y. S. Kivshar, Nonlinear optical magnetism revealed by second-harmonic generation in nanoantennas, Nano Lett. **17**, 3914 (2017).

[23] F. Timpu, A. Sergeyev, N. R. Hendricks, and R. Grange, Second-harmonic enhancement with Mie resonances in perovskite nanoparticles, ACS Photonics **4**, 76 (2017).

[24] C. Ma, J. Yan, Y. Wei, P. Liu, and G. Yang, Enhanced second harmonic generation in individual barium titanate nanoparticles driven by Mie resonances, J. Mater. Chem. C **5**, 4810 (2017).

[25] D. A. Smirnova, A. B. Khanikaev, L. A. Smirnov, and Y. S. Kivshar, Multipolar third-harmonic generation driven by optically induced magnetic resonances, ACS Photonics **3**, 1468 (2016).

[26] K. Thyagarajan, J. Butet, and O. J. F. Martin, Augmenting second harmonic generation using fano resonances in plasmonic systems, Nano Lett. **13**, 1847 (2013)

[27] F. Timpu, N. R. Hendricks, M. Petrov, S. Ni, C. Renaut, H. Wolf, L. Isa, Y. Kivshar, and R. Grange, Enhanced second-harmonic generation from sequential capillarity-assisted particle assembly of hybrid nanodimers, Nano Lett. **17**, 5381 (2017).

[28] Y. Pavlyukh, J. Berakdar, and W. Hubner, Semi-classical approximation for second-harmonic generation in nanoparticles, New J. Phys. **14**, 093044 (2012).

[29] C. F. Bohren and D. R. Huffman, Absorption and scattering by a sphere, *Absorption and Scattering of Light by Small Particles* (John Wiley and Sons, Ltd., 2007), Chap. 4, pp. 82–129.

[30] G. Mie, Contributions to the optics of turbid media, particularly of colloidal metal solutions, Ann. Phys. **330**, 377 (1908).

[31] L.-W. Li, P.-S. Kooi, M.-S. Leong, and T.-S. Yee, Electromagnetic dyadic green's function in spherically multilayered media, IEEE Transactions on Microwave Theory and Techniques **42**, 2302 (1994).

[32] K. A. Fuller, Scattering and absorption cross sections of compounded spheres. I. Theory for external aggregation, J. Opt. Soc. Am. A **11**, 3251 (1994).

[33] S. Cabuk, The nonlinear optical susceptibility and electro-optic tensor of ferroelectrics: First-principle study, Central Eur. J. Phys. **10**, 239 (2012).

[34] S. Chervinskii, K. Koskinen, S. Scherbak, M. Kauranen, and A. Lipovskii, Nonresonant Local Fields Enhance Second-Harmonic Generation from Metal Nanoislands with Dielectric Cover, Phys. Rev. Lett. **120**, 113902 (2018).

[35] S. A. Scherbak and A. A. Lipovskii, Understanding the second-harmonic generation enhancement and behavior in metal core-dielectric shell nanoparticles, J. Phys. Chem. C **122**, 15635 (2018).

[36] M. Celebrano, X. Wu, M. Baselli, S. Großmann, P. Biagioni, A. Locatelli, C. D. Angelis, G. Cerullo, R. Osellame, B. Hecht, L. Duò, F. Ciccacci, and M. Finazzi, Mode matching in

multiresonant plasmonic nanoantennas for enhanced second harmonic generation, Nat. Nanotechnol. **10**, 412 (2015).

[37] K. Thyagarajan, S. Rivier, A. Lovera, and O. J. F. Martin, Enhanced second-harmonic generation from double resonant plasmonic antennae, Opt. Exp. **20**, 12860 (2012).

[38] K. Yang, J. Butet, C. Yan, G. D. Bernasconi, and O. J. Martin, Enhancement mechanisms of the second harmonic generation from double resonant aluminum nanostructures, ACS Photonics **4**, 1522 (2017).

[39] T. Das, P. P. Iyer, R. A. DeCrescent, and J. A. Schuller, Beam engineering for selective and enhanced coupling to multipolar resonances, Phys. Rev. B **92**, 241110 (2015).

[40] E. V. Melik-Gaykazyan, S. S. Kruk, R. Camacho-Morales, L. Xu, M. Rahmani, K. Zangeneh K., A. Lamprianidis, A. E. Miroshnichenko, A. A. Fedyanin, D. N. Neshev, and Y. S. Kivshar, Selective third-harmonic generation by structured light in mie-resonant nanoparticles, ACS Photonics **5**, 728 (2018).

[41] L. D. Landau and E. M. Lifshitz, Chapter XII - the theory of symmetry, *Quantum Mechanics*, 3rd ed. (Pergamon, 1977), pp. 354–395.

[42] M. S. Dresselhaus, G. Dresselhaus, and A. Jorio, *Group Theory. Application to the Physics of Condensed Matter* (Springer, Berlin, Heidelberg, 2008).

[43] V. M. Agranovich and V. Ginzburg, *Crystal optics with spatial dispersion, and excitons*, Vol. 42 (Springer, Berlin, Heidelberg, 2013).

[44] A. G. F. de Beer and S. Roke, Nonlinear Mie theory for second-harmonic and sum-frequency scattering, Phys. Rev. B **79**, 155420 (2009).

[45] D. A. Varshalovich, A. N. Moskalev, and V. K. Khersonsky, *Quantum Theory of Angular Momentum: Irreducible Tensors, Spherical Harmonics, Vector Coupling Coefficients, 3nj Symbols* (World Scientific, Singapore, 1988).

[46] Z. Huayong, H. Yiping, and H. Guoxia, Expansion of the electromagnetic fields of a shaped beam in terms of cylindrical vector wave functions, J. Opt. Soc. Am. B **24**, 1383 (2007).

[47] S. Stein, Addition theorems for spherical wave functions, Q. Appl. Math. **19**, 15 (1961).

[48] Z. Huayong and H. Yiping, Addition theorem for the spherical vector wave functions and its application to the beam shape coefficients, J. Opt. Soc. Am. B **25**, 255 (2008).

[49] R. W. James, New tensor spherical harmonics, for application to the partial differential equations of mathematical physics, Philos. Trans. R. Soc., A **281**, 195 (1976).

[50] G. Aubert, An alternative to Wigner d-matrices for rotating real spherical harmonics, AIP Advances **3**, 062121 (2013).

[51] E. Ivchenko and G. Pikus, *Crystal Symmetry. In: Superlattices and Other Heterostructures.*, Vol. 110 (Springer Series in Solid-State Sciences, Springer, Berlin, Heidelberg, 1995).

[52] Y.-L. Geng, X.-B. Wu, L.-W. Li, and B.-R. Guan, Mie scattering by a uniaxial anisotropic sphere, Phys. Rev. E **70**, 056609 (2004).

[53] B. Stout, M. Nevière, and E. Popov, Mie scattering by an anisotropic object. part i. homogeneous sphere, J. Opt. Soc. Am. A **23**, 1111 (2006).

[54] C. Wong, Y. Y. Teng, J. Ashok, and P. Varaprasad, Barium titanate (batio3), in *Handbook of Optical Constants of Solids*, edited by E. D. Palik (Academic Press, Boston, 1998), pp. 789–803.

[55] S. Wemple, M. Didomenico, and I. Camlibel, Dielectric and optical properties of melt-grown batio3, J. Phys. Chem. Solids **29**, 1797 (1968).

[56] H. Chen, W. Zhang, Z. Wang, and N. Ming, The scattering properties of anisotropic dielectric spheres on electromagnetic waves, J. Phys.: Condens. Matter **16**, 165 (2003).

[57] K. Frizyuk, Second harmonic generation in dielectric nanoparticles with different symmetries, arXiv:1812.02988.

[58] B. Stout, M. Nevière, and E. Popov, Mie scattering by an anisotropic object. Part II. Arbitrary-shaped object: differential theory, J. Opt. Soc. Am. A **23**, 1124 (2006).

[59] S. H. Dong and R. Lemus, The overlap integral of three associated Legendre polynomials, Appl. Math. Lett. **15**, 541 (2002).

[60] S. Hayami, M. Yatsushiro, Y. Yanagi, and H. Kusunose, Classification of atomic-scale multipoles under crystallographic point groups and application to linear response tensors, Phys. Rev. B **98**, 165110 (2018).